JGR Space Physics

RESEARCH ARTICLE
10.1029/2023JA031987

Special Section:
Fifteen Years of THEMIS Mission

Properties of Magnetohydrodynamic Normal Modes in the Earth's Magnetosphere

M. D. Hartinger[1,2], T. Elsden[3], M. O. Archer[4], K. Takahashi[5], A. N. Wright[3], A. Artemyev[2], X. Zhang[6], and V. Angelopoulos[2]

[1]Space Science Institute, Boulder, CO, USA, [2]UCLA Department of Earth, Planetary and Space Sciences, Boulder, CA, USA, [3]Department of Mathematics and Statistics, University of St. Andrews, St. Andrews, UK, [4]Space and Atmospheric Physics Group, Department of Physics, Imperial College London, London, UK, [5]The Johns Hopkins University Applied Physics Laboratory, Laurel, MD, USA, [6]University of Texas at Dallas, Richardson, TX, USA

Abstract The Earth's magnetosphere supports a variety of Magnetohydrodynamic (MHD) normal modes with Ultra Low Frequencies (ULF) including standing Alfvén waves and cavity/waveguide modes. Their amplitudes and frequencies depend in part on the properties of the magnetosphere (size of cavity, wave speed distribution). In this work, we use ∼13 years of Time History of Events and Macroscale Interactions during Substorms satellite magnetic field observations, combined with linearized MHD numerical simulations, to examine the properties of MHD normal modes in the region $L > 5$ and for frequencies <80 mHz. We identify persistent normal mode structure in observed dawn sector power spectra with frequency-dependent wave power peaks like those obtained from simulation ensemble averages, where the simulations assume different radial Alfvén speed profiles and magnetopause locations. We further show with both observations and simulations how frequency-dependent wave power peaks at $L > 5$ depend on both the magnetopause location and the location of peaks in the radial Alfvén speed profile. Finally, we discuss how these results might be used to better model radiation belt electron dynamics related to ULF waves.

Plain Language Summary The solar wind constantly disturbs plasma in the near-Earth space environment on a broad range of frequencies. However, plasma waves in the Earth's magnetosphere, a region of space where the Earth's magnetic field plays a dominant role in shaping plasma dynamics, often exhibit standing wave structure with a narrow range of frequencies. In other words, the magnetosphere selects standing waves with discrete frequencies from drivers with a broadband frequency spectrum. These standing waves have properties that depend on the size of the magnetosphere and plasma wave speeds. In this study, we use a database of magnetic field measurements from the Time History of Events and Macroscale Interactions during Substorms satellites along with numerical simulations to isolate natural frequencies from noisy and variable driving conditions and extract standing wave spatial structure. We show how the standing wave properties change as the outer boundary of the magnetosphere and internal wave speeds change. We finally discuss how the properties of these standing waves might be used to improve space weather models.

Key Points:

- Magnetohydrodynamic normal modes are identified using ∼13 years of observations and comparisons with numerical simulations
- Radial Alfvén speed profile peaks outside 8 Earth radii significantly alter frequencies and spatial structure of normal modes
- Frequencies and nodal structure of cavity/waveguide modes vary with magnetopause location, with power peaks well inside the magnetopause

Supporting Information:

Supporting Information may be found in the online version of this article.

Correspondence to:

M. D. Hartinger,
mhartinger@spacescience.org

Citation:

Hartinger, M. D., Elsden, T., Archer, M. O., Takahashi, K., Wright, A. N., Artemyev, A., et al. (2023). Properties of Magnetohydrodynamic normal modes in the Earth's Magnetosphere. *Journal of Geophysical Research: Space Physics*, *128*, e2023JA031987. https://doi.org/10.1029/2023JA031987

Received 9 AUG 2023
Accepted 6 DEC 2023

1. Introduction

The Earth's magnetosphere supports a wide range of plasma wave modes, with the lowest frequency waves often having spatial scales comparable to the size of the Earth's magnetosphere. These wave frequencies correspond to the lower end of the Ultra Low Frequency (ULF) band, with frequencies <∼100 mHz. At these frequencies, wave properties and dynamics can often be modeled with a magnetohydrodynamic (MHD) approximation (e.g., Southwood & Hughes, 1983). Many observational studies have been performed on ULF waves, with early work leading to a classification scheme based on wave frequency and event duration (Jacobs et al., 1964). For example, Pc3, Pc4, and Pc5 refer to waves that last many wave cycles ("Pc" for pulsations continuous) with frequencies of ∼22–100, ∼7–22, and ∼2–7 mHz, respectively.

Theory, modeling, and ground-based observations of Pc3-5 waves indicate that many of these waves are related to standing MHD waves in the Earth's magnetosphere. Sugiura and Wilson (1964) made an analogy between magnetic field lines and stretched strings to describe the dynamics of standing Alfvén waves. There are several other types of MHD waves that are partially trapped between different boundaries in the Earth's magnetosphere, including radially trapped magnetosonic waves (e.g., reviews by Lee and Takahashi (2006) and Wright and

Mann (2006)). Resonant mode conversion is also possible between standing magnetosonic waves and standing Alfvén waves via the field line resonance mechanism (Kivelson & Southwood, 1986; Southwood, 1974; Tamao, 1965).

These standing or partially standing waves are all generally described as normal modes, or wave modes that exist at a specific set of frequencies (f) and wavelengths (λ) for a specific set of equilibria. In the Earth's magnetosphere, the equilibria correspond to the properties of the region the waves are confined as represented by the radial Alfvén speed profile, magnetopause location, etc. Theory and modeling both confirm that if a driving condition has a spectrum of f and λ, certain normal modes will be excited at certain frequencies (e.g., Degeling et al., 2018; Elsden & Wright, 2019). There are numerous examples of normal modes predicted from theory based on a box model (e.g., Kivelson & Southwood, 1985). In the limit of zero azimuthal wave number, the Alfvén and magnetosonic modes decouple and there exists the toroidal mode (standing Alfvén wave) and cavity mode (magnetosonic mode). In the limit of large azimuthal wave number, there is only the poloidal mode standing Alfvén wave. Later modeling refinements used a waveguide rather than a closed box geometry, leading to the development of another magnetosonic normal mode, the waveguide mode (Samson et al., 1992). Additional model developments related to wave dynamics near the plasmapause led to the concept of the virtual resonance (Lee & Kim, 1999); the virtual resonance model has many similarities to the cavity mode model, but due to different treatments of inner magnetosphere boundary conditions the two models often predict different radial amplitude structure. Still later refinements used more realistic geometries that accounted for magnetic field line curvature and flaring of the magnetopause (Elsden & Wright, 2022; Wright & Elsden, 2020), compressed magnetic field and azimuthally asymmetric wave speeds (Degeling et al., 2010, 2018; Elsden et al., 2022), and local time dependent drivers (e.g., Degeling & Rankin, 2008; Elsden & Wright, 2019).

Observations have confirmed the existence of toroidal modes (e.g., Takahashi et al., 2015) poloidal modes (e.g., Hughes et al., 1978), cavity modes (e.g., Hartinger et al., 2012; Takahashi et al., 2010), waveguide modes (e.g., Mann et al., 1998), and virtual resonances (e.g., Shi et al., 2017) with a range of techniques based on ground-based and/or in situ measurements and in a variety of regions in the Earth's magnetosphere. However, extracting information about normal mode properties from statistical analysis of ULF wave power is complicated by the fact that waves or transients unrelated to normal modes can contribute to wave power spectra at the frequencies of normal modes (e.g., Anderson et al., 1990; Hartinger, Angelopoulos, et al., 2013; Lessard et al., 1999). For example, drift-mirror modes (e.g., Rae et al., 2007) and "breathing modes" (e.g., Di Matteo et al., 2022) can both generate large magnetic variations in the Pc5 frequency range, overlapping with the frequencies of some normal modes in the outer magnetosphere.

There is a strong motivation for separating MHD normal modes from other ULF waves that affect space weather when developing empirical and physics-based models of ULF wave activity. For example, MHD normal modes in the Pc4-5 frequency band (2–22 mHz) have the appropriate frequencies and phase speeds for a variety of drift and drift-bounce interactions with radiation belt and ring current electrons and ions (e.g., Elkington & Sarris, 2016; Elkington et al., 1999; Zong et al., 2017). ULF waves and transients unrelated to normal modes can also significantly affect particle dynamics, but they do so in different ways that do not involve drift resonance. For example, drift-mirror modes with Pc5 frequencies modulate higher frequency ULF and Very Low Frequency wave activity that in turn causes loss or acceleration (e.g., X. J. Zhang et al., 2020). Drift-mirror modes and MHD normal modes are typically combined together in statistical studies of ULF wave power, and the drift-mirror modes may well be expected to dominate statistical analyses in some regions due to their large amplitudes (Zhu & Kivelson, 1991). Thus, it would be advantageous to separate them for the purpose of modeling inner magnetosphere wave-particle interactions.

Statistical studies of ULF wave properties often take one of two tracks: (a) analysis of band-integrated wave power/amplitude for a specific component(s) of electric or magnetic field (e.g., Sandhu, Rae, Wygant, et al., 2021; Sarris et al., 2022; X. J. Zhang et al., 2020) or (b) analysis of occurrence rates of specific wave modes identified using wave polarization, spectral power peaks, etc. (e.g., Hartinger, Angelopoulos, et al., 2013; Murphy et al., 2015; Takahashi & Ukhorskiy, 2007). Despite yielding significant insight into normal mode properties and, more broadly, ULF wave properties needed for radiation belt modeling and other applications, these two approaches have some limitations when it comes to extracting the frequency and spatial dependence of normal modes from measurements. Depending on the bandwidth, the approach to analyze band-integrated wave power can average together multiple harmonics of normal modes thus obscure frequency and spatial dependence, and

it cannot directly distinguish between normal modes and waves/transients unrelated to normal modes that have a broadband frequency spectrum. The approach to analyze occurrence rates is limited by a selection bias that only includes time intervals when the chosen identification criteria are satisfied, thus making it possible that some normal modes are excluded from study and making it difficult to compare occurrence rates across studies that use different selection criteria; for example, Hartinger, Angelopoulos, et al. (2013) could only obtain a lower bound occurrence rate for cavity/waveguide modes due to a sampling bias for quiet conditions when these normal modes could be uniquely identified and sorted from other activity.

Takahashi and Anderson (1992) employed a third approach to statistically characterize frequency and spatial dependent ULF wave activity. They removed background trends from wave magnetic field power spectra and organized them as a function of spatial location and the Kp index, yielding statistically representative wave magnetic field power maps as a function of frequency, local time, radial distance, magnetic latitude, and geomagnetic activity. Their approach afforded sufficient frequency resolution to resolve normal mode structure that compared favorably to numerical simulations (Lee & Lysak, 1989, 1990). However, their results only extended to a radial distance of $L \sim 6$. While there is significant observational evidence that normal modes occur at $L > 6$, it is not clear that their frequency dependent spatial structure can be identified in wave power maps using similar methods as Takahashi and Anderson (1992); there may be too much variability in the properties of normal modes in this region due to the large range of possible equilibria (wave speeds due to variable plasmasphere and ring current, range of magnetopause locations, wave frequencies, etc.), and the normal modes may be obscured by transient disturbances and other wave modes that commonly occur in this region (e.g., Hartinger, Angelopoulos, et al., 2013; Zhu & Kivelson, 1991).

In this work, we expand on earlier efforts by Takahashi and Anderson (1992) to examine normal mode spatial structure, focusing on the region $L > 6$. We compare our observational results with numerical simulations, in each case examining how normal mode properties vary for different sets of magnetospheric equilibria. Our goal is to determine (a) how normal mode properties depend on magnetospheric equilibria (magnetopause location, Alfvén speed profile) and (b) whether normal modes such as cavity/waveguide modes can be captured in statistical wave power results. In Section 2, we describe the methods used for our statistical analysis of satellite magnetometer data and MHD simulations. In Section 3, we show comparisons between observations and simulations for several sets of magnetospheric equilibria. In Section 4, we discuss our results and their implications for radiation belt and ring current modeling. In Section 5, we summarize our results.

2. Methodology

2.1. Data Analysis

2.1.1. Instrumentation

For the observational component of this study, we primarily use measurements from the fluxgate magnetometer (FGM) instrument on the five-satellite Time History of Events and Macroscale Interactions during Substorms (THEMIS) mission (Angelopoulos, 2008; Auster et al., 2008). FGM data from 3 of 5 THEMIS satellites with typical apogees near 12 Earth radii are used to obtain wave power spectral densities over a ∼13 year period from 1 February 2008 to 1 December 2020; the other two satellites are less useful for this study as they entered lunar orbit in 2010. In addition to FGM, we use plasma moments from the Electrostatic Analyzer (ESA, McFadden, Carlson, Larson, Ludlam, et al., 2008) and spacecraft potential. The plasma moments are used primarily for data reduction, while spacecraft potential is used for inferring electron density to obtain information on radial Alfvén speed profile peaks. We also use geomagnetic activity indices and propagated solar wind measurements from NASA's Space Physics Data Facility OMNIWeb interface hourly database. The solar wind measurements are primarily used to determine the magnetopause location using the Shue et al. (1997) model.

2.1.2. Data Processing and Reduction

We follow many of the data processing and data reduction steps of Hartinger, Angelopoulos, et al. (2013) and Hartinger, Moldwin, et al. (2013). The initial data processing and calibration were conducted using the open-source SPEDAS software (Angelopoulos et al., 2019) version 3.1. We follow the same procedure for each of three THEMIS spacecraft: THEMIS-E, THEMIS-D, and THEMIS-A. First, we remove data when the satellite is in eclipse or when particle (ESA) and/or magnetic field measurements have a gap based on data products

generated onboard the spacecraft. Next, magnetosheath periods are identified when the satellite is at a radial distance >8 Earth radii and one or more of the following conditions are met: electron density >10/cc, perpendicular electron number flux is $>2 \times 10^7$ num/cc/s, or velocity is <−200 km/s in the GSM x direction. We then reduce the data set by restricting to periods when (a) the satellite is in the magnetosphere and not the magnetosheath and (b) the satellite is at a radial distance $4.8 < r < 13.5$ Re. The rationale for (a) and (b) is that we are only interested in magnetospheric normal modes in this study, 4.8 Re is just outside the location where magnetometer range changes usually occur (it is usually not possible to measure small amplitude normal modes when the magnetometer is in a high range mode near perigee) and 13.5 Re is close to or exceeds the maximum apogee of the THEMIS-A, D, and E satellites. Once we identify periods that meet these three criteria, we further require that they are at least 55 min in length to ensure a 1,024 point Discrete Fourier Transform (DFT) can be conducted (51 min DFT window plus two minutes on either side to account for magnetosheath transitions). During each of these intervals, spacecraft potential is used to infer electron density (Laakso & Pedersen, 1998; McFadden, Carlson, Larson, Bonnell, et al., 2008). The electron densities are then combined with magnetic field measurements from FGM to obtain the Alfvén speed by assuming a proton plasma. During each data interval, the radial distance with maximum Alfvén speed is recorded. We refer to this as x_{ib} as in Archer et al. (2017), who associated it with the inner boundary of an outer magnetosphere cavity and linked it to effects on normal mode properties. We also compare our x_{ib} results with those from an empirical model from Archer et al. (2017), as discussed in Section 3.2.

Calibrated, spinfit magnetic field measurements are obtained from FGM in SM coordinates. The data are interpolated to have uniform 3 s time resolution, and spikes due to instrumentation artifacts are removed. Gaps in the magnetic field measurements smaller than 12 s are interpolated; DFT windows with larger gaps are removed from the analysis. Prior to obtaining wave power spectral densities, the magnetic field data are rotated into mean field aligned (MFA) coordinates where a single mean value for the magnetic field is obtained separately for each DFT window; as noted by Di Matteo and Villante (2018), this approach avoids artifacts such as artificial discrete frequency wave power peaks that would be introduced with, for example, a running mean value that changes inside the DFT window. In the MFA coordinate system, z is along the magnetic field direction, $x = \phi_{SM}$ x z where ϕ_{SM} is the azimuthal direction in SM coordinates, and y completes the right hand orthogonal set. In addition to the coordinate transformation, we also remove slowly varying trends to better examine wave fields. For this purpose, we fit a third order polynomial to the data contained within the DFT window and subtract this polynomial from the original magnetic field measurements for the x, y, and z components separately. Here, again, we use the same polynomial for the entirety of the 1,024 point DFT window to avoid artifacts in the resulting power spectra (Di Matteo & Villante, 2018). Finally, wave power spectral densities are obtained. To reduce uncertainties, wave power is calculated for two DFT windows that are half the length of the broader 1,024 point window, and these wave power results are averaged together. Uncertainties are further reduced by averaging over three adjacent frequency bins resulting in the final wave power spectral density estimates. Figure S1 in Supporting Information S1 shows an example THEMIS-E satellite interval used in the database.

The steps above are repeated for the three THEMIS spacecraft that spend the most time in the Earth's magnetosphere during the ∼13-year interval we considered: THEMIS-A, THEMIS-D, and THEMIS-E. The spacecraft sample somewhat different regions during different mission phases, though they yield similar results in the context of this study (e.g., Figure S2 in Supporting Information S1) and are combined together to form the final wave power database. This results in a database with 1,984.2, 2,070.9, and 2,033.2 days of useable magnetic field wave power data from THEMIS-A, THEMIS-D, and THEMIS-E respectively, for a total of 6,088.3 days or 171,234 wave power spectra. For a single spacecraft, each day corresponds to roughly 28 DFT windows that do not overlap in time, thus 84 DFT windows are obtained each day when measurements from the three spacecraft are combined. Though our focus will be on wave power results from 1,024 point DFT windows, a second database was constructed using 512 point DFT to determine whether the DFT window length significantly affected the results; as was the case for the 1,024 point DFT, uncertainties in the wave power estimates are reduced by applying a three point smooth over frequency and two point average in time. No significant differences were found between the two databases, apart from the expected decrease in frequency resolution and increase in data coverage. The 1,024 point DFT with three point smooth resulted in samples from 0.70 to 160 mHz with a frequency bin spacing of 2.0 mHz whereas the 512 point DFT with three point smooth resulted in 1.3–160 mHz with a 3.9 mHz spacing. One example comparison between the 512 and 1,024 point DFT results is shown in Figure S1c and S1d in Supporting Information S1, which show that results from the 512 point DFT window compare well with the

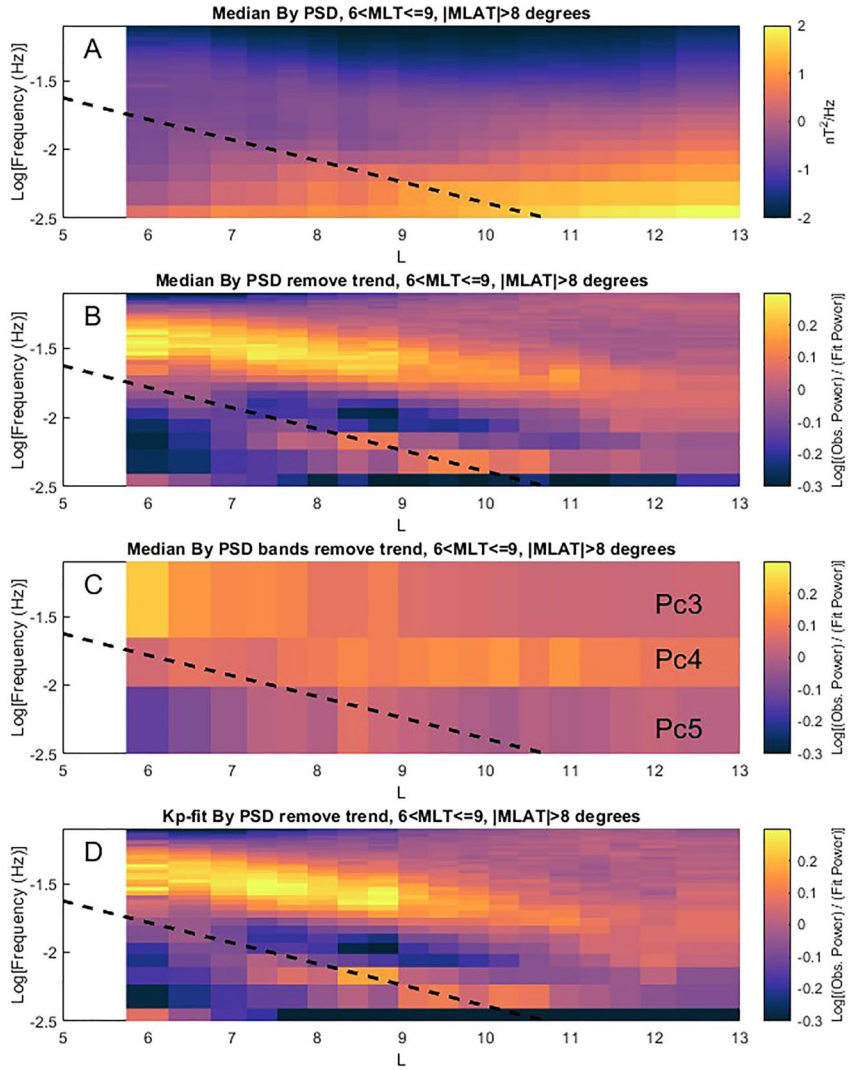

Figure 1. Example statistical results for the *y* component of the magnetic field in the 6 < MLT ≤ 9 sector and for magnetic latitudes greater than 8°. (a) Median wave power in color as a function of frequency on the *y*-axis and radial distance on the *x*-axis. (b) The same data as (a), but in this case background trends are removed from each power spectrum prior to taking the median. (c) The same data as (a), but background trends are removed and mean values for the Pc5, Pc4, and Pc3 band are taken prior to taking the median. (d) The same data as (a), but in this case the result of robust fit of wave power to Kp at Kp = 20 is shown rather than the median value. In each panel, a dashed black line indicates the predicted standing Alfvén wave frequency (fundamental mode).

1,024 point DFT window (both panels show the presence of standing Alfvén waves). Note that 1,024 point DFT windows correspond to ~0.9 Re of spacecraft radial motion near 6 Re and <~0.1 Re near perigee, whereas 512 point DFT windows correspond to ≤0.5 Re near 6 Re and <~0.05 Re near perigee.

The parameters stored in the wave database include SM position of each sample (center of DFT window) and wave power for the three components of the magnetic field in MFA coordinates. The database is publicly available (Hartinger, 2023).

2.1.3. Statistical Analysis Methods

We use median values for statistical analysis of wave power spectral density observations as they are less likely to be skewed by extreme values. Figure 1a shows median wave power (units of $\frac{nT^2}{Hz}$) as a function of frequency and dipole L for magnetic local times (MLT) from 6 < MLT ≤ 9 and magnetic latitudes (MLAT) > 8°. In the remainder of this manuscript we focus on 6 < MLT ≤ 9 for three main reasons: (a) the radial Alfvén speed profile

has somewhat less variability in this sector (Archer et al., 2015, 2017) allowing us to reduce factors we need to control for and so we can use relatively simple statistical analysis methods (i.e., median value), (b) normal modes are expected to be prevalent in this local time sector (Archer et al., 2015, 2017; Takahashi et al., 2015), and (c) for brevity, as describing the normal mode properties in all local time sectors in both simulations and data requires an extremely lengthy manuscript and is beyond our intended scope. Note that while our wave database includes data at $r > 4.8$ Re, the L-value of the first DFT sample shown in Figure 1a starts at >∼5.5. This is primarily because of the spacecraft motion effect described at the end of Section 2.1.2. A hypothetical 1,024 point DFT window that began the moment an outbound spacecraft crossed $L \sim 4.8$ would have a start and stop L-value of ∼4.8 and ∼6. Since the spacecraft's radial velocity decreases as it moves outward, the L-value at the center time of this DFT window will be closer to 6 than to 4.8.

In Figure 1a, a black dashed line is for qualitative expectations for the fundamental mode standing Alfvén wave frequency (toroidal mode) using a time of flight approximation from the Appendix of Chi and Russell (1998) that assumes a dipole magnetic field, the Carpenter and Anderson (1992) electron density model, and an assumption of an average ion mass of 1.5 amu. These calculations are used for simplicity as they are only needed for qualitative comparisons with observations needed to identify fundamental toroidal modes, but they are similar to those obtained from more sophisticated calculations based on observed electron densities and more realistic magnetic field models (e.g., Archer et al., 2015). At $L > 9$, these frequencies are also similar to observed toroidal mode frequencies by Takahashi et al. (2015) (Figure 11a in that study for the $4 < \text{MLT} < 8$ sector), while at $L < 9$ they are a ∼2–4 mHz higher. Note the spread in observed frequencies can be quite large, for example, ranging from ∼2–20 mHz at $L \sim 6$ in the $4 < \text{MLT} < 8$ sector (Figure 11a of Takahashi et al. (2015)).

The most prominent feature in Figure 1a is the gradually increasing wave power with increasing radial distance at most frequencies (brighter colors at the right of the panel) and gradually decreasing wave power with increasing wave frequency (brighter colors at the bottom of the panel). These trends are consistent with past studies generally showing increased wave power at higher radial distances (e.g., X. J. Zhang et al., 2020) and lower frequencies (e.g., Takahashi & Anderson, 1992). A wave power trend following the dashed black curve for standing Alfvén waves is less clear, apart from faintly visible power enhancements seen most clearly at higher frequencies. This is no longer the case in Figure 1b; here, robust least squares regression is used to obtain a fit between the logarithm of wave power and the logarithm of frequency for each individual DFT window using the form $\text{Log10(Power)} = A*\text{Log10(Frequency)} + B$ (equivalent to a power law if not in logspace). This fit to the logarithm of wave power is subtracted from the original spectra prior to taking the median value. The median wave power shown in Figure 1b thus reflects discrete frequency peaks associated with normal modes rather than background trends in power due to disturbances with more broadband frequency content (e.g., transients, drift-mirror modes). Note that Figure 1b and all subsequent wave power observations are dimensionless as subtracting the wave power trend in logspace is equivalent to obtaining the logarithm of the ratio of observed wave power to the wave power trend. Discrete frequency peaks that approximately follow the expected trend for fundamental mode standing Alfvén waves are now visible (compare dashed black curve to band of orange/yellow color) as well as higher harmonics, most likely dominated by the third and fifth harmonics (odd harmonics are expected to be prevalent off the magnetic equator for externally driven toroidal modes), that are likely mixed together on this plot (band of orange/yellow color that extends across much of the plot with a trend of gradually decreasing frequency as L increases). Note that the plasmapause is typically expected at $L < 6$ (O'Brien & Moldwin, 2003).

Figure 1c shows the same data as in the second panel, but mean wave power in the wider Pc5, Pc4, and Pc3 frequency bands is shown to illustrate how averaging or integrating across the frequency band removes information about the normal mode spatial structure; this point will be discussed further in Section 4. Finally, Figure 1d shows the result of a least squares fit of wave power to the Kp index at each frequency and spatial location (the result for a Kp value of 20 is shown, using the representation of Kp without decimal points from Matzka et al. (2021)), similar to the approach taken by Takahashi and Anderson (1992) and the approach used by many radiation belt studies to obtain radial diffusion coefficients by first identifying relationships between ULF wave power and Kp, frequency, and L (e.g., Brautigam et al., 2005; Fei et al., 2006). As in Figures 1b and 1c the wave power in Figure 1d is normalized to a background trend, following the procedure of Takahashi and Anderson (1992); unlike in Figures 1b and 1c and the rest of this study, the background power trend is obtained for the statistical results of wave power versus frequency rather than for individual DFT windows (see Takahashi and Anderson (1992) Section 3.3 for further details). Though there are some small differences in wave power values, the results of the fit to Kp appear very similar to the median values (compare Figures 1b and 1d). A Kp

Table 1
Summary of the Numerical Simulations Used in This Study

Description	Va radial gradient	Local Va peak	Subsolar magnetopause
1 - Shallow Va, Small Lmp	Shallow	None	$L = 10$
2 - Moderate Va, Small Lmp	Moderate	None	$L = 10$
3 - Steep Va, Small Lmp	Steep	None	$L = 10$
4 - Shallow Va, Medium Lmp	Shallow	None	$L = 11$
5 - Moderate Va, Medium Lmp	Moderate	None	$L = 11$
6 - Steep Va, Medium Lmp	Steep	None	$L = 11$
7 - Shallow Va, Large Lmp	Shallow	None	$L = 12$
8 - Moderate Va, Large Lmp	Moderate	None	$L = 12$
9 - Steep Va, Large Lmp	Steep	None	$L = 12$
10 - Peak Va 6, Medium Lmp	N/A	$L = 6$	$L = 11$
11 - Peak Va 9, Medium Lmp	N/A	$L = 9$	$L = 11$

value of 20 is larger than the median value in our database but it is representative, and the results shown in Figure 1d do not change significantly if values of 10, 13, or 17 are used instead of 20. Note that the median Kp obtained for the entire period from 1 February 2008 to 1 December 2020 is 13, while the median value in our database is slightly lower at 10 due to the removal of larger Kp events which often coincide with conditions when the THEMIS satellite is outside the magnetopause near apogee (we require THEMIS be inside the magnetosphere for a DFT window to be recorded since we are studying magnetospheric ULF waves).

In the remainder of this study, for simplicity we will only analyze wave power measurements using median values obtained after the subtraction of power law trends from individual spectra (i.e., like Figure 1b). This will allow us to focus on normal mode spatial structure and frequency rather than absolute amplitudes that may be dominated by transient magnetic disturbances, drift-mirror modes, and other magnetic disturbances with broadband frequency spectra. We note that our general conclusions hold when using a variety of methods (e.g., Figure 1d), and that many of the MHD normal mode features we describe are visible in median power spectra with no trend removal, though they are faint (e.g., the higher harmonic standing Alfvén waves in Figure 1a described above).

2.2. Numerical Simulations

We employ the numerical model of Wright and Elsden (2020), which solves the linear MHD equations for a cold plasma in a background dipole magnetic field. Full details of the model, including detailed descriptions of testing and the various choices made in the code development are given by Wright and Elsden (2020), with only the key properties summarized here. The model uses orthogonal, field-aligned coordinates (α, β, γ), permitting high resolution both along and across the magnetic field. For comparison with the observations the coordinates correspond to the following directions: $\mathbf{e}_\gamma$ is the field-aligned direction, referred to as $\mathbf{e}_\parallel$; $\mathbf{e}_\beta$ is the azimuthal direction, notated by $\mathbf{e}_\phi$; $\mathbf{e}_\alpha$ gives the outward normal direction on a given field line, but will be compared to the $\mathbf{e}_\mathbf{r}$ direction from the observations. The simulation coordinates $\mathbf{e}_\mathbf{r}$, $\mathbf{e}_\phi$, and $\mathbf{e}_\parallel$ are analagous to the data coordinates x, y, and z.

The simulation domain is designed to study the dayside magnetosphere. The outer sunward boundary of the simulation is given by the location of the magnetopause in the equatorial plane using the Shue et al. (1997) model, from where the model is driven. The inner earthward boundary is set at $L = 5$, with a perfectly reflecting (node of radial velocity) boundary condition modeling a sharp change in the density at the plasmapause. The propagation of waves into the magnetotail is modeled with a dissipative region beyond $X = -6\ R_E$ (for X along the Earth-Sun line), such that waves which propagate into the tail do not return to the dayside solution region of interest. Only the northern hemisphere is solved for, with a symmetry condition applied at the equator for numerical efficiency, given that the model is driven symmetrically about the equator. The ionospheric boundary is further treated as reflecting. Dissipation is provided in the domain through the inclusion of resistivity to prevent small scales which develop through Alfvén wave phase mixing dropping below the grid resolution. The magnetopause boundary in all of the simulations presented here is driven in the same way, with continuous broadband perturbations (~0–50 mHz) to the field-aligned magnetic field component $B_\parallel$. By driving in the same way in each simulation, we are able to compare the effect of the equilibrium (magnetopause location and density) on the wave solutions.

We have performed 11 simulations to be discussed in this manuscript, with the different setup criteria summarized in Table 1. Using three different subsolar magnetopause locations (L_{mp} = 10, 11, 12), and three Alfvén speed radial profiles with different gradients (shallow to steep, see Figure S3 in Supporting Information S1), yields nine simulations. Two further runs consider the effect of localized peaks in $V_A(L)$ at different L. Figure 2 gives an example output from the simulations, displaying the wave power at different frequencies of the azimuthal magnetic field B_ϕ as a function of L-shell, along the meridian MLT = 8 and off the equator (see Figure S7 in Supporting Information S1). The quantity shown in this figure and subsequent simulation figures is the logarithm (base 10) of the magnitude of the DFT coefficient which has the units of nT; it is proportional to wave power. Note that the units of data figures (base 10 logarithm of the power ratio) and simulation figures (base 10 logarithm of the DFT magnitude in units of nT) differ, and they should not be compared quantitatively.

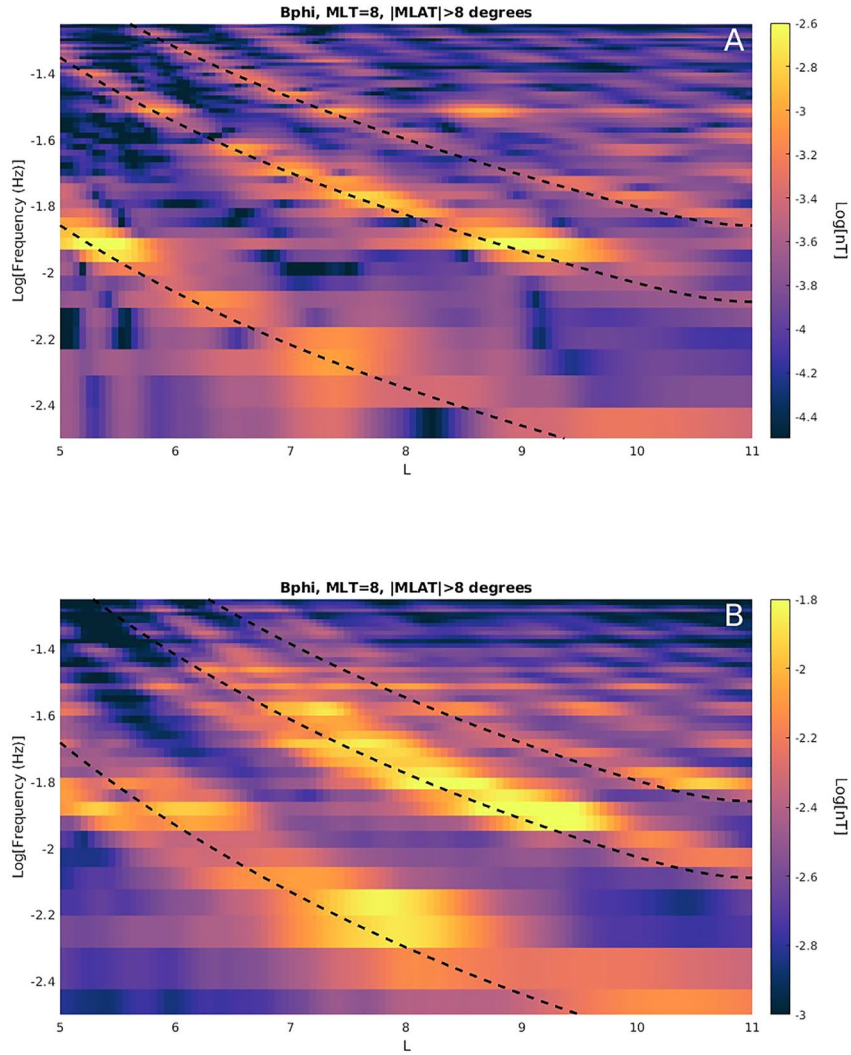

Figure 2. (a) Simulated meridional wave power for the ϕ component of the magnetic field in the MLT = 8 meridian averaged for magnetic latitudes greater than 8°; the results shown correspond to a single simulation, number 4 in Table 1, with dashed lines indicating the first, second, and third harmonic standing Alfvén wave frequencies. (b) The same format as panel (a) but instead showing the average of an ensemble of nine simulations (Numbers 1–9 in Table 1), including the simulation in panel (a). In this case, the dashed lines are averages of the standing Alfvén wave frequencies calculated for the three different Alfvén speed profiles reflected in the simulation ensemble. The individual results for each of the nine simulations are shown in Figures S4–S6 in Supporting Information S1.

The rationale for our choice for the range $V_A(L)$ was motivated by past studies of $V_A(L)$ including Archer et al. (2015) (e.g., statistical results in Figure 1g in that study) and Archer et al. (2017) (e.g., examples in Figure 2 in that study), as well as visual inspection of $V_A(L)$ from events examined in our database. The values for $V_A(L)$ used in the simulations aren't representative of any single event, but rather they are meant to qualitatively explore trends in wave trapping, reflection, etc. due changing gradients and presence/absence of $V_A(L)$ peaks that are reasonable based on observations. The L_{mp} values used in the simulations are also meant to be representative of past studies of L_{mp} location and the range of L_{mp} in our database predicted by the Shue et al. (1997) model (the most likely L_{mp} in our database predicted by Shue et al. (1997) is 10.9 Earth radii); here, again, the range of values chosen is meant to qualitatively explore trends in normal mode structure while also being representative of typical observed L_{mp} values. For both $V_A(L)$ and L_{mp}, we do not attempt to simulate extreme cases (e.g., 99% of L_{mp} values lie between 6.7 and 13.2 Earth radii) though that is an important topic for future work. When more accurate information becomes available for $V_A(L)$ profiles (e.g., most work, including the present study, uses electron density observations with an assumed ion composition to obtain mass density thus $V_A(L)$) and better

constraints on particular values for radial gradients, peak locations, etc., these should also be incorporated in future simulations for more direct, quantitative comparisons with observations. For example, while we have drawn from examples from case studies (e.g., Archer et al., 2017; Figure 2) and median statistical profiles (e.g., Archer et al., 2015; Figures 1g and 1h) to estimate the size and width of $V_A(L)$ peaks, it is likely that the properties of $V_A(L)$ peaks vary significantly from event to event depending on event-specific ion composition, plasmaspheric plume structure, etc.

Figure 2a is for a single simulation, with $L_{mp} = 11$ and weak V_A radial gradient. Dashed lines indicate the expected first, second, and third harmonic standing Alfvén wave frequencies calculated using simulation parameters (wave speeds); these lines compare very well with wave power enhancements, consistent with the presence of multiple standing Alfvén wave harmonics in this simulation. Figure 2b is an average of nine simulations for the different permutations of the three magnetopause locations and three $V_A(L)$ gradients; in this case, the dashed lines are averages of the calculated standing Alfvén wave frequencies for the three different Alfvén speed profiles reflected in the simulation ensemble. Clear frequency bands are present showing the different harmonics in both panels, but in Figure 2b these bands are somewhat blurred due to the averaging across the different simulations. Figures S4–S6 in Supporting Information S1 show results for each of the nine simulations used in the average. Note that we are using average, or arithmetic mean, values for ensemble analysis of simulation measurements as there are too few simulation runs to obtain meaningful median values. Throughout the rest of the study, we will use median values to represent the distribution of observed wave power values in different conditions and spatial regions (previous section), while mean values will serve the same purpose for ensemble simulation runs. The use of these two different quantities will not affect our conclusions as we only rely on qualitative comparisons between simulations and observations.

3. Results

In this section, we examine how different magnetospheric equilibria affect normal mode properties using both observations and numerical simulations, focusing on two parameters that are known to control ULF wave properties (Section 1): magnetopause location and radial Alfvén speed profile. We will also analyze results for a broader set of conditions as a point of reference.

3.1. Results for a Broad Range of Conditions

Figure 3 is for average values from an ensemble of nine simulations with different magnetopause locations and radial Alfvén speed gradients (simulations 1–9 in Table 1, see Figure S3 in Supporting Information S1 for radial Alfvén speed profiles); the results for individual simulations are shown in Figures S4–S6 in Supporting Information S1. Figures 3a–3c is for the MLT = 8 meridian and regions near the magnetic equator (magnetic latitude less than 5°); average wave power is shown in color as a function of frequency (y-axis) and radial distance (x-axis) for the radial (Figure 3a), azimuthal (Figure 3b), and parallel (Figure 3c) magnetic field components. In Figure 3b, discrete frequency peaks are seen with frequency that decreases with increasing radial distance as expected for standing Alfvén waves. In Figure 3c, discrete frequency peaks appear that are consistent with expectations for cavity/waveguide modes, including (a) the local minima and maxima in wave power as a function of radial distance that differ from expectations for surface waves and disturbances originating from the magnetopause which would have monotonically decaying wave power with distance from the magnetopause and (b) the constant frequency with radial distance that differs from expectations for standing Alfvén waves. Though the features in Figures 3a–3c are consistent with normal modes, they are blurred together consistent with the ensemble average. The lowest frequency peak in Figure 3c has a radial structure consistent with a quarter wavelength cavity/waveguide mode, in particular a power peak near the inner boundary of the simulation. This is due to the use of a perfectly reflecting boundary condition at $L = 5$ (node in radial velocity, anti-node or peak in parallel magnetic field).

Figures 3d–3f is the same as Figures 3a–3c but for regions off the magnetic equator (magnetic latitude greater than 8°) and using a different colorbar to account for larger wave power in some panels. In particular, discrete frequency wave power in the azimuthal magnetic field seen in Figure 3e is significantly larger than in Figure 3b as expected for odd harmonics of toroidal mode standing Alfvén waves. As before, however, the features are blurred together. These results can be compared against Figures S4–S6 in Supporting Information S1 which show much

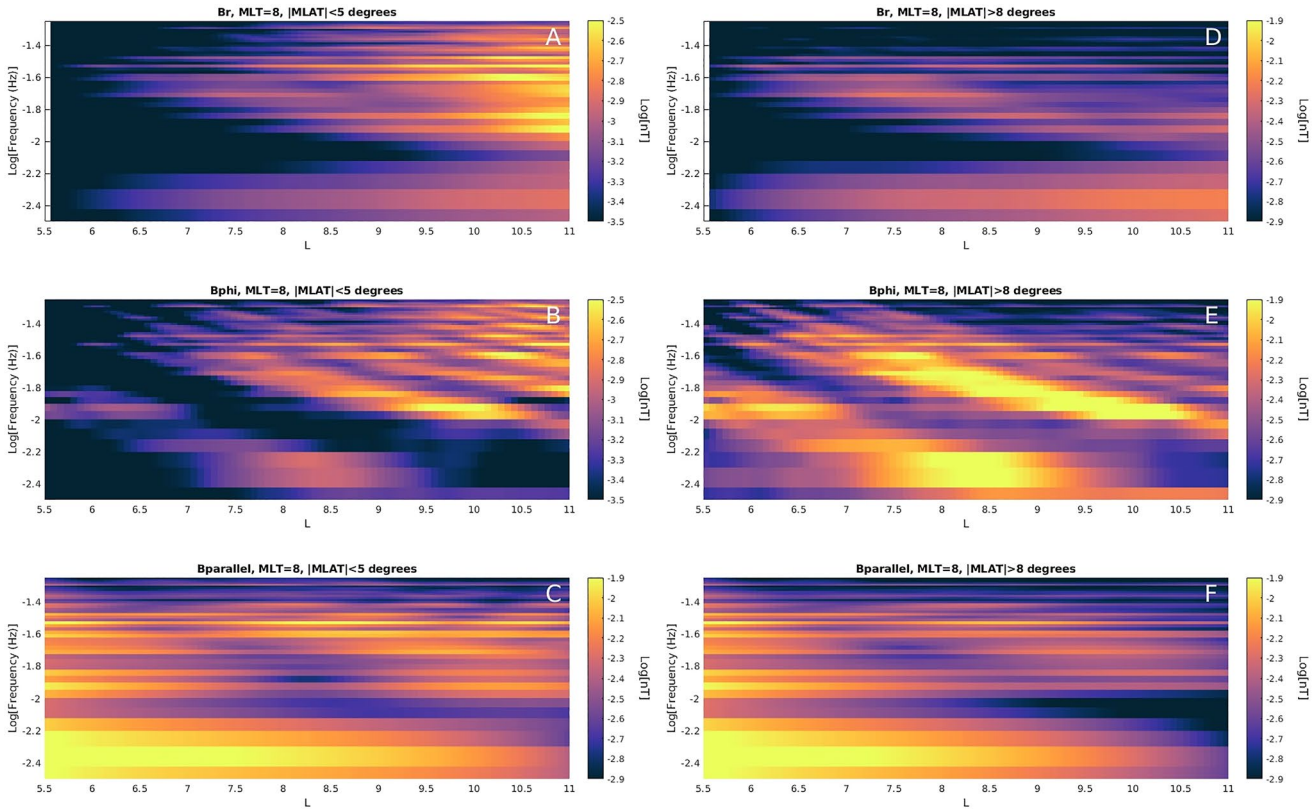

Figure 3. Ensemble average simulation results (simulations 1–9 in Table 1). (a) Wave power along the MLT = 8 meridian on the magnetic equator (|MLAT| < 5°) for the magnetic variations in the radial magnetic field. (b) The same as (a), but for azimuthal magnetic field. (c) The same as (a), but for the component parallel to the background magnetic field. (d–f) The same as (a–c) but for locations off the magnetic equator (|MLAT| > 8°).

narrower and distinct discrete frequency peaks in the individual simulations that make up the average shown in Figure 3.

The results in Figure 3 are qualitatively consistent with what might be expected when statistically analyzing wave measurements that include a range of different driving conditions. However, it is not obvious whether similar trends would be seen in observations at higher *L*-values near the magnetopause given expectations in that region for significant variability in the radial Alfvén speed profile (Archer et al., 2015), magnetopause geometry (Shue et al., 1997), and the presence of drift-mirror modes and other magnetic disturbances unrelated to normal modes (Zhu & Kivelson, 1991). Figure 4 shows that, despite the presence of this variability, median wave power spectra can indeed reveal normal mode structure and are at least qualitatively consistent with the simulations. In particular, Figures 4a–4c is in the same format as Figures 3a–3c, showing median wave power as a function of radial distance (*x*-axis) and frequency (*y*-axis) for regions near the magnetic equator (magnetic latitude less than 5°). From top to bottom, results are shown for the radial (Figure 3a), azimuthal (Figure 3b), and parallel (Figure 3c) magnetic field, and a dashed line in all panels indicates the expected frequency for a fundamental toroidal mode using the same approximation as in Figure 1. In Figure 4b, two broad peaks in wave power are observed above the predicted fundamental mode frequency (dashed line) that blur together at low radial distances. Both peaks have frequency decreasing with increasing radial distance, consistent with standing Alfvén waves. These peaks have frequencies that are consistent with second and third harmonic toroidal waves. Little power is observed at frequencies expected for fundamental mode standing Alfvén waves (dashed line), consistent with the expected location of a node (local minima) in wave power near the magnetic equator (Sarris et al., 2022; Sugiura & Wilson, 1964). The blurring of these features that becomes more pronounced at smaller radial distances is due at least in part to the increase in the variation of eigenfrequencies closer to the Earth (e.g., Archer et al., 2015; Takahashi et al., 2015).

Figure 4c is for the parallel magnetic field component, with two broad, constant frequency peaks in wave power observed that include local minima and maxima as a function of radial distance. As was the case with the

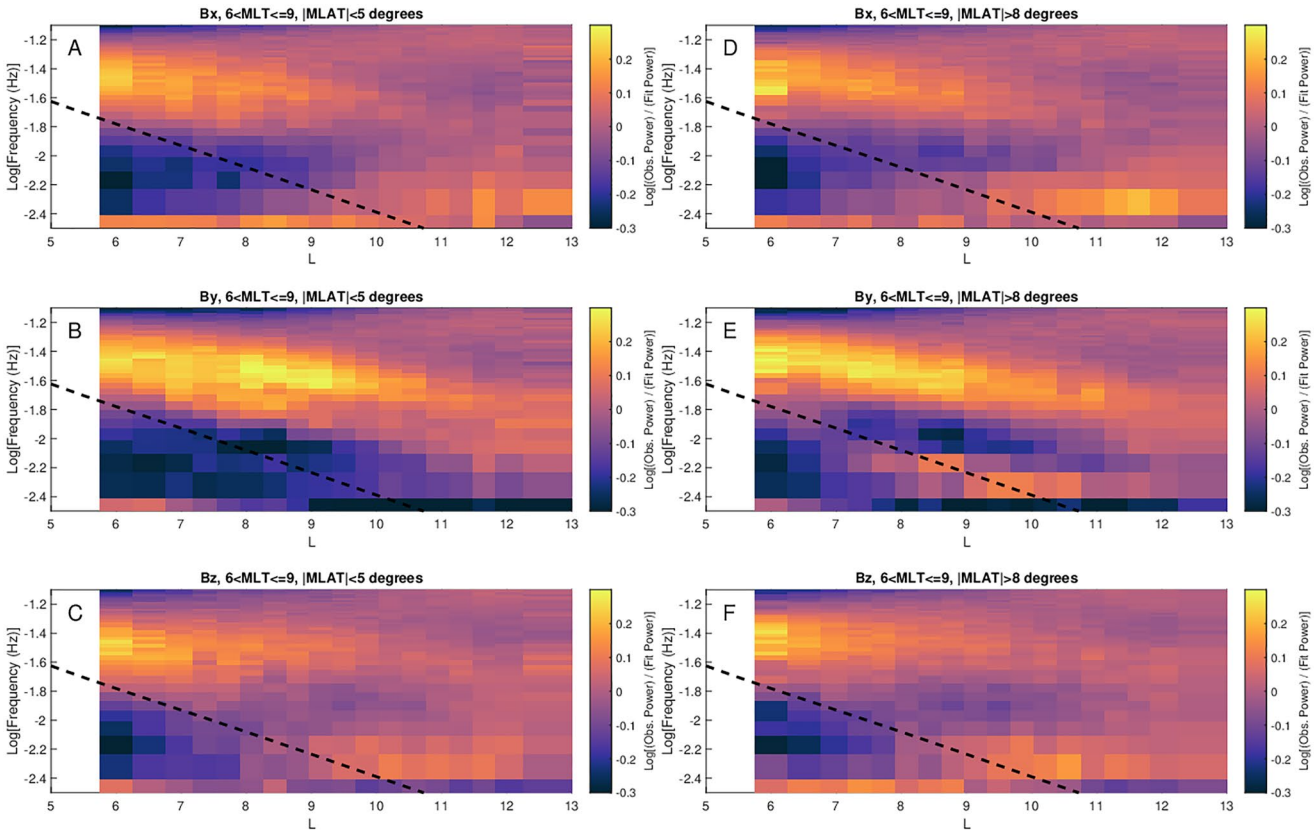

Figure 4. (a) Median wave power in the x component (radial in mean field aligned coordinates) in the $6 < \text{MLT} \leq 9$ sector and for magnetic latitudes less than 5°. A dashed black line indicates the predicted standing Alfvén wave frequency (fundamental mode). (b) The same as (a), but for the y component (azimuthal). (c) The same as (a), but the z component (parallel to background magnetic field). (d–f) The same as (a–c) but for locations off the magnetic equator ($|\text{MLAT}| > 8°$).

simulations, these features are consistent with cavity/waveguide modes, with the blurred features suggesting that there is significant variability in the frequency of cavity/waveguide modes reflected in the median values. Concerning the higher frequency peak, the blurring and general preference for a subset of the Pc3-4 frequency band may also be due in part to the energy source(s) for these waves. For example, upstream waves (waves associated with the ion foreshock) have a finite bandwidth that usually extends across much of the Pc3-4 range; though magnetospheric waves associated with upstream waves are generally expected to have maximum amplitudes close to the outer boundary, magnetospheric cavity modes with peak compressional magnetic field perturbations deep inside the magnetosphere similar to what's seen in Figure 4c can also be driven by upstream waves (Takahashi et al., 2010). One would generally expect to see a mixture of the driving energy spectrum and the normal modes in these plots. The compressions seen in Figure 4c may also be due in part to poloidal mode Alfvén waves which are known to be associated with magnetic compressions in realistic magnetic field geometries (e.g., Dai et al., 2015). The lower frequency peak in Figure 4c is also likely associated with a cavity/waveguide mode, though, as with the higher frequency peak, it may well include contributions from other wave modes such as magnetopause surface waves associated with the Kelvin-Helmholtz instability and magnetopause surface eigenmodes which can have frequencies that extend into the Pc5 range (Plaschke & Glassmeier, 2011). In Section 3.3, we will show conclusively that both of these features, while including some contributions from other wave modes, exhibit behavior that can only be related to normal modes.

Figures 4d–4f is the same as the Figures 4a–4c but for locations off the magnetic equator (magnetic latitude greater than 8°). The most significant difference appears in Figure 4e, where a discrete frequency peak in wave power is seen that matches the expected frequency dependence of the fundamental toroidal mode (wave power enhancement near dashed black line). As was the case for the simulations, the much larger wave power in the fundamental mode off the magnetic equator is expected for the odd mode structure with node in magnetic field perturbation at the magnetic equator. It is also consistent with trends seen in recent observational work examining

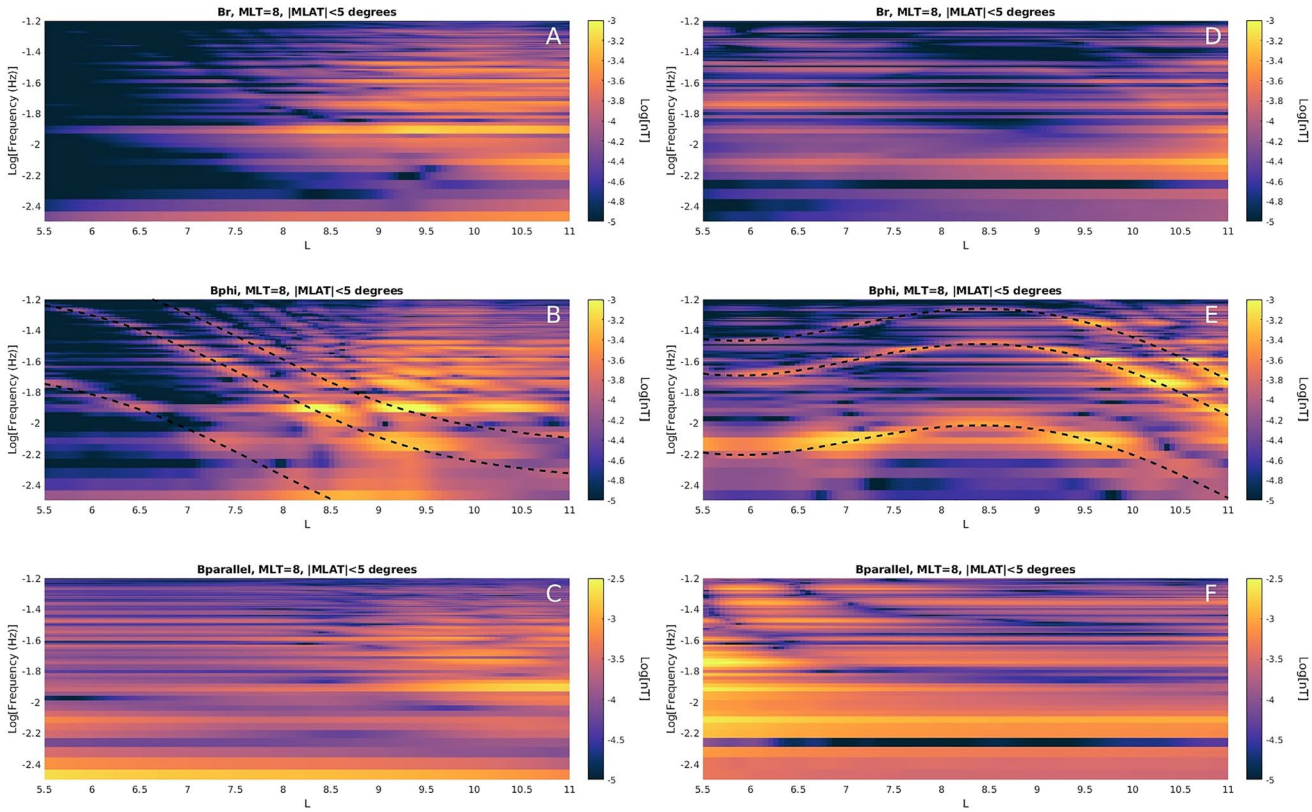

Figure 5. (a) Wave power results in the radial component are shown for the MLT = 8 sector and magnetic latitudes less than 5° for a simulation where a local peak in the radial Alfvén speed profile is at a radial distance of 6 R_E. (b) The same as (a), but for the azimuthal component. Dashed lines are for calculated standing Alfvén wave frequencies for the first, second, and third harmonics. (c) The same as (a), but for the component parallel to the background magnetic field. (d–f) The same as for (a–c), but results are shown for a simulation where the local peak in the radial Alfvén speed profile is at 9 R_E.

band-integrated wave power (e.g., Sarris et al., 2022). The fact that the peak in power along this dashed line is just inside the location with peak Pc5 power in Figure 4c that was associated with a cavity/waveguide mode (see above) further suggests that cavity/waveguide modes may be coupling to toroidal modes via field line resonance to produce these features. It's also worth noting that in contrast to the two peaks in power above the predicted fundamental mode frequency that were seen in regions close to the magnetic equator (Figure 4b), only the highest frequency peak is seen in Figure 5e; this is further evidence that the lower frequency peak seen in Figure 4b was consistent with a second harmonic mode, as a lower amplitude is expected for this mode off the magnetic equator. Finally, the peaks in power in Figure 4f have some similarities to Figure 4c; these are likely caused by the same types of wave activity, though perhaps with different relative contributions from the Alfvén mode, cavity/waveguide mode, etc. Note that both Figures 4c and 4f do not have the peak in power at low frequencies near $L = 5$ seen in the simulations (compare with Figures 3c and 3f); this is likely due to the use of a perfectly reflecting inner boundary at $L = 5$ in the simulations, as discussed above.

Taken together, Figures 3 and 4 show that normal modes can be sustained in the magnetosphere in a wide range of conditions, but due to having properties that vary from event to event they are blurred together in statistical analysis when examining median values that include all conditions. The presence of more discrete frequency peaks and smaller spatial scale features in the ensemble average simulation output (Figure 3) reflects the fact that we have only run nine simulations where variability is only represented by three different radial Alfvén speed profiles and three different magnetopause locations. If we had incorporated, for example, 1,000 simulations with wider range of conditions the features would invariably blur further and be more consistent with the observations in Figure 4. Nevertheless, Figure 4 shows that normal mode structure is evident even in median wave power spectra; this is somewhat remarkable when considering the variability expected in this region, for example, in the magnetopause location (Murphy et al., 2015; Sandhu, Rae, Staples, et al., 2021; Shue et al., 1997), radial Alfvén speed profile (Archer et al., 2015; Sandhu, Rae, Staples, et al., 2021; Wharton et al., 2019), and other parameters.

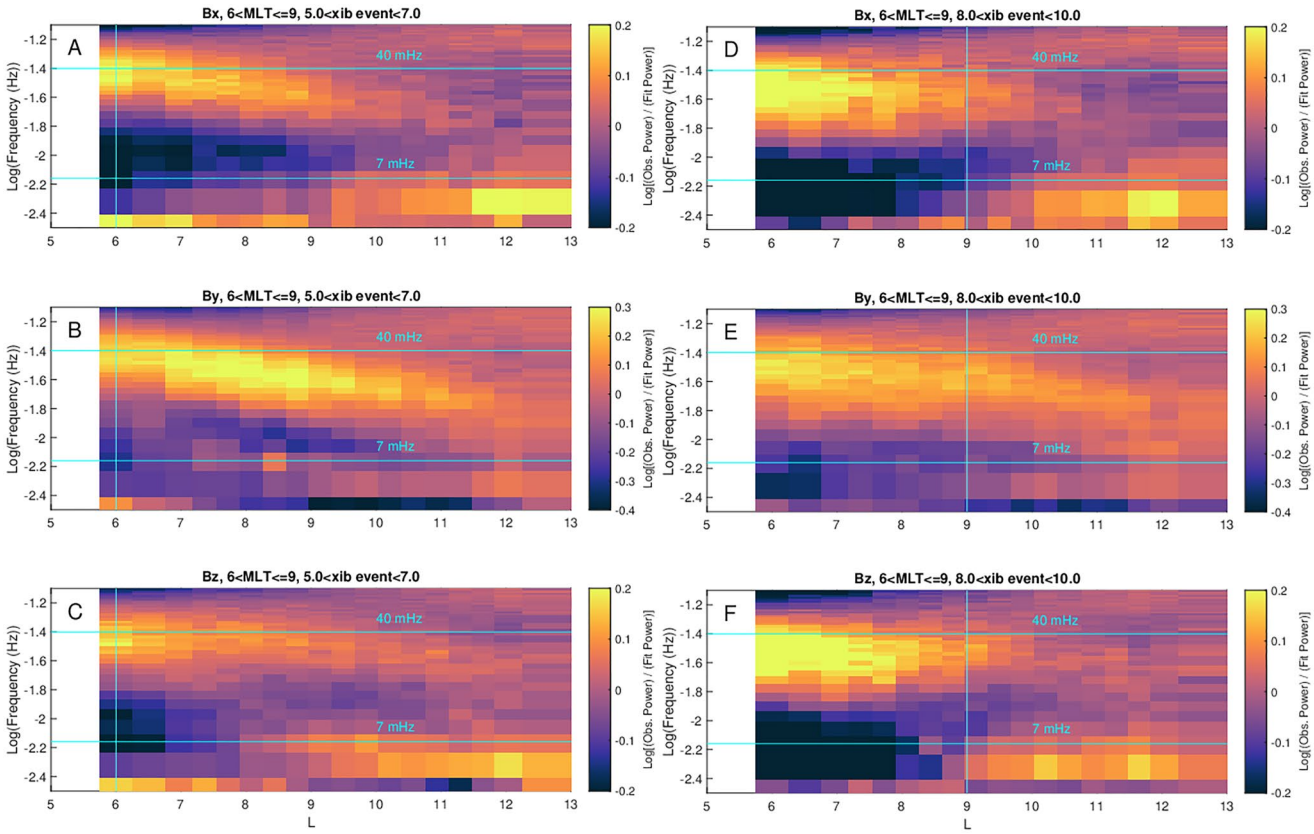

Figure 6. (a) Median wave power in the x component (radial in mean field aligned coordinates) in the $6 < \text{MLT} \leq 9$ sector and conditions where the local maximum in the radial Alfvén speed profile, x_{ib}, is in the range $5.0 < x_{ib} < 7.0$. A vertical blue line marks the center of the range of x_{ib} values, 6.0 R_E, while horizontal dashed lines are shown at values of 7 and 40 mHz. (b) The same as (a), but for the y component (azimuthal). (c) The same as (a), but the z component (parallel to background magnetic field). (d–f) The same as (a–c), but for $8.0 < x_{ib} < 10.0$. The vertical blue line is now at 9 R_E, the center of the x_{ib} range.

3.2. Different Radial Alfvén Speed Profiles

The numerical simulations in Section 3.1 used radial Alfvén speed profiles that decreased monotonically with increasing radial distances throughout the simulation domain. In this section, we consider profiles with local peaks (x_{ib} location) at 6 and 9 Re (radial Alfvén speed profiles shown in Figure S7 in Supporting Information S1). Figures 5a–5c is the same format as the Figures 3a–3c (MLT = 8, magnetic latitude less than 5°), but for a single simulation where the Alfvén speed profile has a peak near the inner boundary at $L = 6$ Re; as was the case in Figure 3, discrete frequency peaks are seen in Figure 5b with decreasing frequency as radial distance increases, though the frequency varies more slowly near the Alfvén speed peak at $L = 6$ (compare Figure 3b to Figure 5b). Dashed lines in Figure 5b are for the frequencies calculated for the first, second, and third standing Alfvén harmonics using the Alfvén speeds in the simulations; the close correspondence between these lines and the discrete frequency power enhancements provides further evidence for the presence of standing Alfvén waves. Figures 5d–5f is for the case where the local Alfvén speed peak is at $L = 9$ Re. This significantly alters the normal mode structure in several ways: (a) the frequency of all normal modes changes, (b) the standing Alfvén wave frequency first increases, then flattens, then decreases with increasing radial distance when the peak is at larger L-values (compare Figures 5b and 5e), (c) the maxima in wave power for radial (Figures 5a and 5d) and compressional (Figures 5c and 5f) components changes location, with significant wave power trapped inside the location of the Alfvén speed peak when located at $L = 9$ (Figure 5f).

Figure 6 is for median wave power for situations when x_{ib} (peak Alfvén speed in each data segment, see Section 2) is at $5 < x_{ib} < 7$ Re (Figures 6a–6c) or $8 < x_{ib} < 10$ Re (Figures 6d–6f). For comparison, Figure S8 in Supporting Information S1 obtains x_{ib} using the empirical model of Archer et al. (2017), with similar results. The same MLT region is shown as in Figures 4a–4c ($6 < \text{MLT} \leq 9$), but, unlike in Figure 4, all MLAT are included to obtain enough data for meaningful statistical results. There are 22,350 samples (DFT windows) in this local time sector, with 8,405 (37.6%) and 5,120 (22.9%) samples in the $5 < x_{ib} < 7$ and $8 < x_{ib} < 10$ Re bins, respectively; thus, these locations

for x_{ib} occur frequently in this sector. This is consistent with results from past work, including Archer et al. (2017) and the empirical modeling of Moore et al. (1987) which nominally puts the dawn sector peak at ~7 Re (Figure 2a in that study), though as noted in Section 2 there is considerable variability in peak location from event to event.

As in Figure 4, Figures 6a–6c exhibits evidence of normal modes: (a) discrete frequency peaks with decreasing frequency as radial distance increases in the middle panel consistent with standing Alfvén waves and (b) constant frequency peaks with nodes/anti-nodes in the bottom panel consistent with cavity/waveguide modes. Similar evidence of normal modes is also found in Figures 6d–6f ($8 < x_{ib} < 10$), but there are significant differences now that x_{ib} is at higher radial distances: (a) significant wave energy in the radial (Figure 6d) and parallel (Figure 6f) magnetic field found inside the peak location at frequencies in the Pc4 and lower Pc3 frequency ranges with comparatively less power in the outer magnetosphere, (b) less Pc5 wave energy in the parallel magnetic field at low radial distances when x_{ib} is at large radial distances (i.e., decreased ability for fast mode waves at lower frequencies to penetrate to the inner magnetosphere, compare Figure 6c to Figure 6f), and (c) the discrete frequency peaks that were seen in the azimuthal magnetic field (Figure 6b) are much broader and only exhibit a clear trend of decreasing frequency with increasing radial distance at radial distances larger than the radial Alfvén speed peak ($L > \sim 10$ Re).

The simulations in Figure 5 and the data in Figure 6 both show consistent changes in normal mode properties as the local peak in the radial Alfvén speed profile changes location: (a) flat or non-monotonically decreasing standing Alfvén wave frequencies when there's a peak at larger radial distance, (b) increased compressional wave trapping in the inner magnetosphere (inside the Alfvén speed peak) when the peak is at larger radial distances. There are some differences between the data and simulations, likely because (a) we are comparing statistical results against individual simulations rather than an ensemble of simulations and (b) the simulated Alfvén speed profiles and inner boundary location are not fully representative of nominal conditions in the magnetosphere. Nevertheless, taken together, these results show that theoretical predictions for the alteration of MHD normal mode structure in the presence of different radial Alfvén speed peak locations are consistent with the data. Conditions with $x_{ib} > 6.0$ Earth radii occur frequently in the outer magnetosphere (Archer et al., 2015, 2017) and should be considered more carefully in space weather models that rely on ULF wave fields (see Section 4).

3.3. Different Subsolar Magnetopause Locations

In this section, we consider how subsolar magnetopause location affects MHD normal mode structure. As in previous simulation figures, Figure 7 shows wave power in the MLT = 8 meridian as a function of radial distance on the x-axis and frequency on the y-axis. Here, all panels are for MLAT below 5° and for wave power in the parallel component of the magnetic field. Figure 7a is identical to Figure 3c and is for the ensemble average of simulations 1–9 in Table 1, including conditions where the subsolar magnetopause is at 10, 11, and 12 Re; it is shown for reference to compare against simulations for specific magnetopause locations. Figure 7b is for an average of simulations 1–3 in Table 1, all of which have a subsolar magnetopause at 10 Re. Though appearing qualitatively similar to Figure 7a, there are a few differences: (a) no simulation output (white space) in outermost L-values due to the flank magnetopause moving inward, (b) sharper discrete frequency peaks in wave power with somewhat different peak power locations when compared to the top panel, (c) overall more wave power at low L-values. Figure 7c is for an average of simulations 4–6 in Table 1, all of which have subsolar magnetopause locations at 11 Re. As with Figure 7b, the discrete frequency peaks in wave power are overall sharper than in Figure 7a. Additionally, the peak wave power locations have shifted somewhat when compared to Figures 7a and 7b. Similar differences are again seen in Figure 7d which is for an average of simulations 7–9 in Table 1, all of which have subsolar magnetopause locations at 12 Re. Comparing Figures 7b–7d, one other trend is obvious as the subsolar magnetopause is shifted outward: a tendency for discrete frequency peaks to shift to lower frequencies as the magnetopause moves outward, seen most obviously when comparing the lowest frequency peaks in each panel. Taken together, the results in Figure 7 show that normal modes in the compressional magnetic field (cavity/waveguide/virtual resonance) exist for all magnetopause locations, but their properties change as the magnetopause location changes: generally decreasing frequency with increasing magnetopause location and changing location of nodes/anti-nodes. The lower frequency with larger magnetopause location is expected due to (a) the larger magnetopause cavity and (b) the smaller magnetic field, thus Alfvén speed, expected when the magnetopause located is further out and the magnetosphere is less compressed (Archer et al., 2017).

Figure 8 tests whether the trends in Figure 7 can be seen in data. Figure 8a shows median wave power in the parallel component of the magnetic field as a function of radial distance on the x-axis and frequency on the

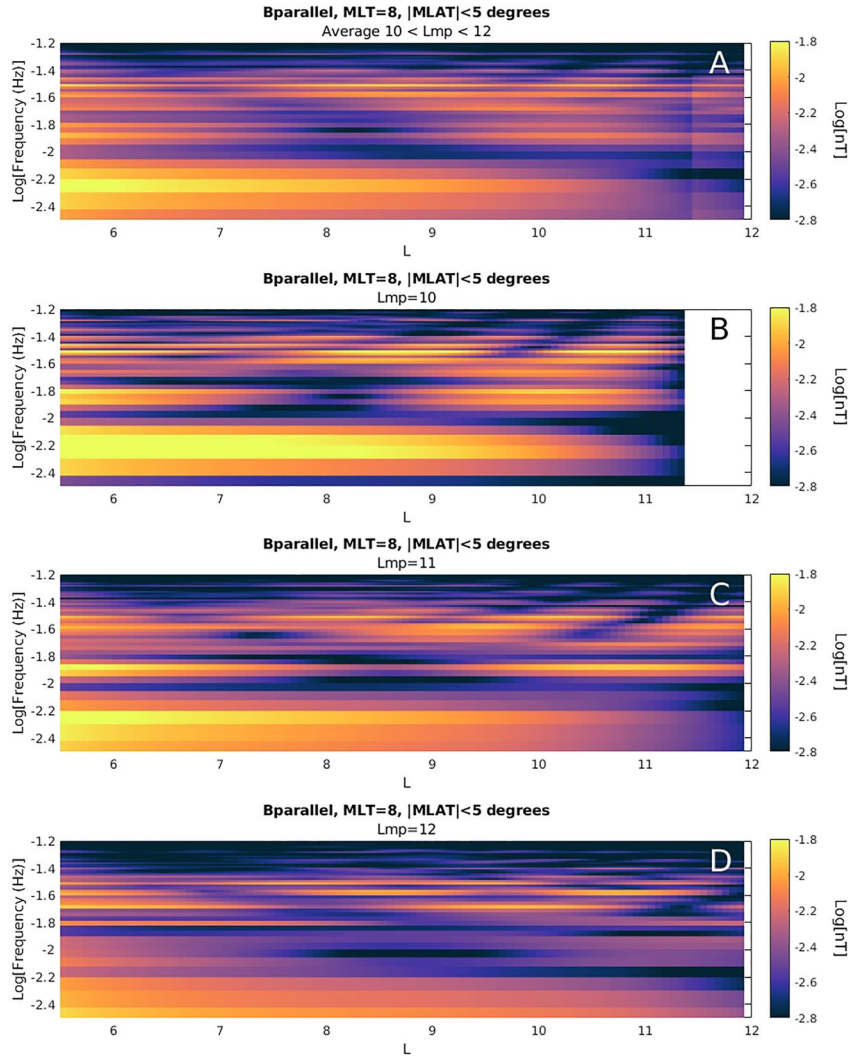

Figure 7. (a) Average wave power in the parallel component of the magnetic field across simulations 1–9 in Table 1; the results are shown as a function of radial distance in the MLT = 8 sector and for magnetic latitudes below 5°. (b) The same as (a), but the average wave power is only calculated using simulations with subsolar magnetopause at $L = 10$ (1–3 in Table 1). (c) The same as (a), but the average wave power is only calculated using simulations with subsolar magnetopause at $L = 11$ (4–6 in Table 1). (d) The same as (a), but the average wave power is only calculated using simulations with subsolar magnetopause at $L = 12$ (7–9 in Table 1).

y-axis in the $6 < \text{MLT} \leq 9$ sector; horizontal and vertical blue lines are for reference as discussed below. The results are similar to Figure 4c, except that all MLAT are included in order to be consistent with other panels (as in Figure 6, this is needed to ensure sufficient data coverage). As discussed in Section 3.1, evidence of cavity/waveguide modes is seen in the form of discrete frequency peaks in wave power with nodal structures that do not change their frequency as radial distance changes. Figure 8b is for median wave power when the subsolar magnetopause obtained from the Shue et al. (1997) model is between 8.5 and 10 Re. Discrete frequency peaks are again seen but with different frequencies and different locations of nodes and anti-nodes. The horizontal blue lines mark the approximate center frequencies of two harmonics, and the vertical line marks the approximate radial distance of the anti-node (local maxima) associated with the lower frequency harmonic; these lines are also shown in other panels to highlight changes in frequency and spatial structure as the magnetopause location changes. Figure 8c is for median wave power when the subsolar magnetopause is between 10 and 11.5 Re; compared with Figure 8b, the frequencies have shifted lower and the anti-node has moved outward. These trends continue in Figure 8d, which is for median wave power when the magnetopause is between 11.5 and 13.5 Re; the frequencies of the harmonics have shifted lower, with anti-nodes at still higher radial distances. Figure 8

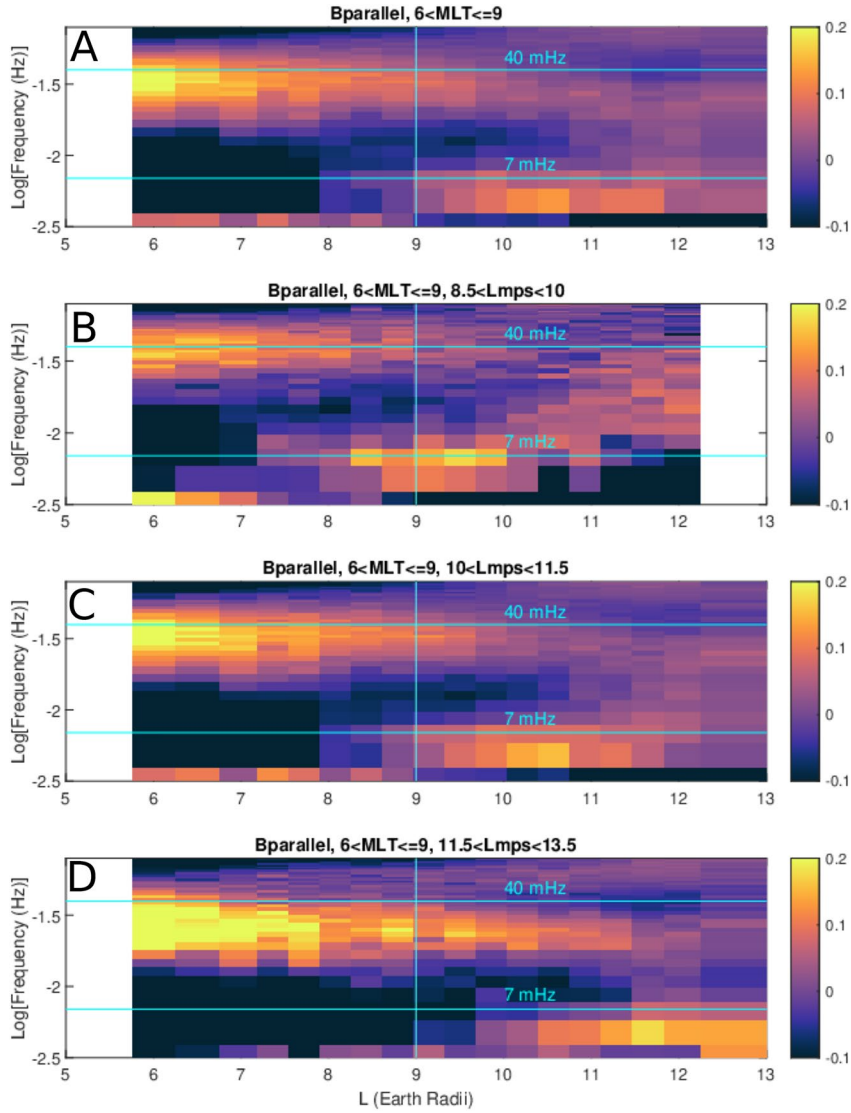

Figure 8. (a) Median wave power in the parallel magnetic field component as a function of radial distance in $6 < \text{MLT} \leq 9$ sector. A vertical blue line marks 9.0 R_E, while horizontal dashed lines are shown at values of 7 and 40 mHz. (b) The same as (a), but only including measurements during conditions when the subsolar magnetopause as determined by the Shue et al. (1997) model is in the range $8.5 < L_{mp} < 10.0$. (c) The same as (b), but for $10.0 < L_{mp} < 11.5$. (d) The same as (b), but for $11.5 < L_{mp} < 13.5$.

provides firm evidence of cavity/waveguide modes in the outer magnetosphere; transient disturbances and other MHD wave modes could not explain these discrete frequency peaks with nodal structure and properties (location of nodes, frequencies) that change according to magnetopause location. Note that the bins chosen for subsolar magnetopause location are consistent with the typical range of values seen in the data set; there are 22,350 DFT samples in the $6 < \text{MLT} \leq 9$ sector, with 2,562 (11.5%), 14,335 (64.1%), and 5,073 (22.7%) samples occurring when $8.5 < L_{mp} < 10.0$, $10. < L_{mp} < 11.5$, and $11.5 < L_{mp} < 13.5$, respectively. However, the exact choice of bin range for L_{mp} is somewhat arbitrary (e.g., 13.0 could have been used instead of 13.5 without changing the results) with the main criteria being (a) that there were sufficient samples in each bin to explore the L variation of normal mode structure and (b) that the bins were sufficiently different that changing normal mode structure due changing L_{mp} could be observed. Future work exploring quantitative comparisons between observations and simulations should adjust these bin ranges and the corresponding simulation outer boundary location for better agreement.

Taken together, the results in Figures 7 and 8 show how the location of the magnetopause affects the properties of MHD normal modes. In contrast to results found for band-integrated ULF wave power in past studies (Section 1),

normal mode amplitudes do not decay monotonically with distance from the magnetopause, and a smaller subsolar magnetopause does not always mean normal mode wave power will be larger at smaller radial distances. When considering whether wave amplitude associated with cavity/waveguide modes will be larger at a given frequency and radial distance, one needs to consider the interplay between the amount of energy being delivered to the normal mode and the frequency and spatial dependence of the normal mode structure. For example, a key difference between the simulation results in Figure 7 and the observed results in Figure 8 is that power enhancements tend to occur near 40 mHz in the observations, whereas in the simulations there is no clear preference near 40 mHz. It is possible that the observed power enhancements near 40 mHz are related to upstream wave activity in the ion foreshock (Takahashi et al., 1984); this energy source is not present in the simulations which use an energy source with a broadband frequency spectrum. Thus, though observations and simulations both indicate normal mode activity with frequency and spatially dependence on magnetopause location, the observations are also affected by a frequency dependent energy source.

4. Discussion

In this study, we statistically analyzed wave power spectra from magnetic field measurements made by the THEMIS satellites and compared with individual and ensemble average numerical simulation results. We identified frequency and spatial-dependent normal mode structure in the region $5 < L < 13$ consistent with theoretical expectations for MHD normal modes. It is somewhat remarkable that these features, while blurred somewhat compared to numerical simulations, are apparent in observed median wave power spectra when considering the variability in normal mode properties expected in magnetopause location, radial Alfvén speed profile, and driving condition, all of which control their frequency and spatial structure. We further showed how the properties of standing Alfvén waves and cavity/waveguide modes changed when restricting to specific magnetopause locations and specific locations of radial Alfvén speed profile peaks, finding significant changes in locations of nodes/antinodes, frequencies, and other properties.

The results presented in Section 3.2 show that the properties of the radial Alfvén speed profile, represented by the x_{ib} parameter corresponding to the radial distance of the peak Alfvén speed at $L > 5$, significantly impact both standing Alfvén wave properties and cavity/waveguide mode properties. Trends observed in numerical simulations (Figure 5) as the peak moves outward such as the flattening/blurring of the radial dependence of standing Alfvén wave frequency and the trapping of compressional wave energy are also qualitatively seen in the data (Figure 6). Past theoretical and numerical simulation work showed that the location of x_{ib}, along with wave frequency and spatial scale, affects the trapping of wave energy and ability to penetrate from the outer magnetosphere to the inner magnetosphere. All things equal, lower frequency waves become evanescent at larger radial distances than higher frequency waves. This is seen in Figure 6; as x_{ib} is moved outward (compare left to right panel), wave power in the radial (top panel) and parallel (bottom panel) components at frequencies below 7 mHz is reduced. This suggests that x_{ib} could be used to organize wave measurements more effectively than, for example, the electron density plasmapause.

The results presented in Section 3.3 show that the magnetopause location - already known to affect a variety of ULF wave properties—affects not only the frequency (e.g., Murphy et al., 2015; D. Zhang et al., 2023) but also the spatial structure of cavity/waveguide modes in the outer magnetosphere. This was expected from theoretical predictions and numerical simulations (e.g., Figure 7), but direct observational evidence of this changing spatial structure was missing likely due to (a) the relatively small amplitudes of cavity/waveguide modes in the outer magnetosphere making them less obvious in case studies or statistical analysis that includes other ULF waves (Hartinger, Angelopoulos, et al., 2013), (b) the lack of a large data set needed to achieve meaningful statistics at a wide range of radial distances and for subsets of magnetopause locations, and (c) the frequency resolution needed to resolve the changing frequency and node/antinode locations (Figure 8) which could not be seen with band-integrated power in, for example, the Pc5, Pc4, and Pc3 ranges (e.g., Figure 1).

These results have potentially important implications for space weather models seeking to capture the effects of MHD normal modes on inner magnetosphere particle populations. Magnetospheric Pc4-5 waves (2–22 mHz) have the appropriate frequencies and phase speeds for drift and drift-bounce interactions with radiation belt electrons (e.g., Elkington et al., 2003; Zong et al., 2017). When a continuum of wave frequencies/modes are present, this radial transport can be described via a diffusion approximation, with several models employing numerous methods for parameterizing the wave fields via radial diffusion coefficients (Drozdov et al., 2021; Lejosne &

Kollmann, 2020; Ozeke et al., 2014). For example, Fei et al. (2006) show that the diffusion coefficients depend in part on wave power at different frequencies and azimuthal wave numbers; radial diffusion coefficient formulations such as in Fei et al. (2006) are in effect assuming MHD waves with phase speeds comparable to relativistic electron drift speeds. However, in practice the techniques used to obtain wave power are not designed to separate these waves—including normal modes which are usually invoked as the mechanism causing drift resonance (e.g., Elkington et al., 1999, 2003; Zong et al., 2017) - from other magnetic disturbances that are not in resonance. This is undesirable for two related reasons:

1. Other ULF wave modes affect radiation belt dynamics in different ways from normal modes thus should ideally not be included in radial diffusion coefficient formulations based on wave power observations. For example, drift-mirror modes do not satisfy drift resonance as they drift at speeds far lower than typical relativistic electron drift speeds. Instead, these compressional waves transport populations of hot, anisotropic ions and electrons, naturally unstable to electromagnetic ion cyclotron (EMIC) waves (e.g., Kitamura et al., 2021) and whistler-mode waves (Watt et al., 2011; Xia et al., 2016; X.-J. Zhang et al., 2019). This ULF wave coupling with EMIC and whistler-mode waves is the main mechanism responsible for quasi-periodic wave dynamics (L. Li et al., 2022; W. Li et al., 2011; Xia et al., 2020) that further controls quasi-periodic electron resonant scattering and subsequent precipitation-related loss (Artemyev et al., 2021; Bashir et al., 2022; Shi et al., 2022).
2. Other ULF wave modes and transients with a more broadband frequency spectrum can have large amplitudes (e.g., Hartinger, Angelopoulos, et al., 2013; Zhu & Kivelson, 1991) relative to normal modes and may dominate trends in statistical analysis of band-integrated wave power. This is undesirable in studies seeking to determine how normal mode properties vary according to changing driving conditions for the purpose of obtaining radial diffusion coefficients or, more broadly, for understanding the driving mechanisms of particular ULF wave modes. For example, Pc5 band-integrated compressional wave power—encompassing a range of phenomena such as drift-mirror waves, magnetopause surface waves, cavity/waveguide modes, transient increases/decreases in magnetic field—generally decreases with increasing distance from the magnetopause, but more narrowband wave activity associated with MHD normal modes does not necessarily follow this pattern, with local maxima occurring well inside the magnetopause (e.g., Figure 8).

Separating normal modes from other sources of ULF wave power would thus be advantageous for developing empirical models of ULF wave power needed to obtain radial diffusion coefficients. The results in this study and Takahashi and Anderson (1992) suggest that wave spectra with background trends removed, validated against numerical simulations, are one tool for addressing this objective. However, more work is needed to determine how MHD normal mode wave power varies under different driving conditions and in different spatial regions, as has been done for ground and space observations of ULF wave power more broadly (e.g., Bentley et al., 2018, 2020; Takahashi & Ukhorskiy, 2007).

5. Summary

We used ∼13 years of THEMIS satellite magnetic field observations, combined with MHD numerical simulations, to examine the properties of MHD normal modes in the region $L > 5$ and for frequencies <80 mHz, focusing on the dawn local time sector. We examine median wave power from detrended spectra as a function of spatial location (radial distance, magnetic latitude), frequency, magnetopause location, and Alfvén speed profile peak (x_{ib}). Our findings are summarized as follows:

1. We identify persistent normal mode structure in observed power spectra with frequency-dependent wave power peaks like those obtained from ensemble simulation averages, where the simulations assume different radial Alfvén speed profiles and magnetopause locations. This is somewhat surprising given the known variability in the outer magnetosphere in radial Alfvén speed profile structure, variable driving conditions, and the presence of other wave modes with larger amplitudes, all of which may have been expected to obscure or blur normal mode properties in median power spectra.
2. The properties of the normal modes, including rapid changes in frequency, are closely tied to the magnetopause location and radial Alfvén speed profile peaks.
3. Shifting the local Alfvén speed profile peak into the outer magnetosphere breaks the assumption of monotonically decaying Alfvén speed with increasing radial distance that is assumed in most theory and modeling work. This changes several MHD normal mode properties: more compressional wave power trapped

earthward of the Alfvén speed peak at Pc3-4 frequencies, less compressional wave power able to penetrate the inner magnetosphere at Pc5 frequencies, non-monotonically varying Alfvén frequencies.

4. Persistent cavity/waveguide mode power peaks occur well inside the magnetopause and have frequencies that vary with magnetopause location.
5. MHD normal modes do not always follow the same trends as seen in past ULF wave statistical studies examining band-integrated wave power, likely due in part to the presence of other wave modes (e.g., drift-mirror mode) or the averaging out of frequency-dependent normal mode structure.

In Section 4 we discuss how these results could be use to improve radiation belt models affected by isolating normal modes from other wave modes and transients prior to obtaining statistical wave power results and related radial diffusion coefficients. Future work should examine how MHD normal mode properties are affected in a wider range of internal and external driving conditions and at more locations. Additionally, more work is needed to compare these results to results obtained from ground-based radars and magnetometers to better understand how normal modes are modified by ionospheric and ground conductance, thus improve ground-based remote sensing techniques and develop understanding of other space weather impacts of normal modes such as geomagnetically induced currents (e.g., Heyns et al., 2021; Hartinger et al., 2023).

Data Availability Statement

The geomagnetic activity indices and solar wind parameters are publicly available at the NASA Space Science Data Facility (https://omniweb.gsfc.nasa.gov/). The THEMIS ULF wave database used to generate the data Figures in this manuscript is publicly available on the Zenodo repository (Hartinger, 2023), while the data used to generate the simulation Figures are publicly available on the figshare repository (Elsden, 2023). All THEMIS data were accessed via the SPEDAS software and are publicly available at the THEMIS Berkeley data repository (http://themis.ssl.berkeley.edu/index.shtml). The SPEDAS software package used for processing the data can be obtained from the THEMIS website (http://themis.ssl.berkeley.edu/index.shtml). Wave power spectral densities were obtained using the publicly available "cross_spectrum" IDL software (https://github.com/svdataman/IDL/blob/master/src/cross_spectrum.pro).

Acknowledgments
MDH was supported by NASA 80NSSC19K0127, 80NSSC19K0907, 80NSSC21K1683, 80NSSC21K1677, and 80NSSC23K0903 and NSF AGS-2307204. KT was supported by NASA 80NSSC19K0259 and 80NSSC21K0453. MOA was supported by a UKRI (STFC/EPSRC) Stephen Hawking Fellowship EP/T01735X/1. The research of A.W. was funded in part by Science and Technology Facilities Council (STFC) Grant ST/W001195/1 (UK). T.E. was funded in part by a Leverhulme Early Career Fellowship ECF-2019-155 (UK). AA and XZ were supported by NASA 80NSSC21K0729 and 80NSSC23K0108. We acknowledge support from ISSI Bern through ISSI International Team projects 483 "The Identification And Classification Of 3D Alfven Resonances" and 546 "Magneto-hydrodynamic Surface Waves at Earth's Magnetosphere (and Beyond)." We acknowledge NASA Contract NAS5-02099 and V. Angelopoulos for use of data from the THEMIS Mission. Specifically: C. W. Carlson and J. P. McFadden for use of ESA data; K. H. Glassmeier, U. Auster, and W. Baumjohann for the use of FGM data provided under the lead of the Technical University of Braunschweig and with financial support through the German Ministry for Economy and Technology and the German Center for Aviation and Space (DLR) under Contract 50 OC 0302. We thank the NASA Space Science Data facility for the use of solar wind data and geomagnetic activity indices. For the purpose of open access, the author(s) have applied a Creative Commons attribution (CC BY) to any Author Accepted Manuscript version arising.

References

Anderson, B. J., Engebretson, M. J., Rounds, S. P., Zanetti, L. J., & Potemra, T. A. (1990). A statistical study of Pc 3-5 pulsations observed by the AmMPTE/CCE magnetic fields experiment 1. Occurrence distributions. *Journal of Geophysical Research*, *95*(A7), 10495–10523. https://doi.org/10.1029/JA095iA07p10495

Angelopoulos, V. (2008). The THEMIS mission. *Space Science Reviews*, *141*(1–4), 5–34. https://doi.org/10.1007/s11214-008-9336-1

Angelopoulos, V., Cruce, P., Drozdov, A., Grimes, E. W., Hatzigeorgiu, N., King, D. A., et al. (2019). The space physics environment data analysis system (SPEDAS). *Space Science Reviews*, *215*(1), 9. https://doi.org/10.1007/s11214-018-0576-4

Archer, M. O., Hartinger, M. D., Walsh, B. M., & Angelopoulos, V. (2017). Magnetospheric and solar wind dependences of coupled fast-mode resonances outside the plasmasphere. *Journal of Geophysical Research: Space Physics*, *122*(1), 212–226. https://doi.org/10.1002/2016JA023428

Archer, M. O., Hartinger, M. D., Walsh, B. M., Plaschke, F., & Angelopoulos, V. (2015). Frequency variability of standing Alfvén waves excited by fast mode resonances in the outer magnetosphere. *Geophysical Research Letters*, *42*(23), 10150–10159. https://doi.org/10.1002/2015GL066683

Artemyev, A. V., Demekhov, A. G., Zhang, X. J., Angelopoulos, V., Mourenas, D., Fedorenko, Y. V., et al. (2021). Role of ducting in relativistic electron loss by whistler-mode wave scattering. *Journal of Geophysical Research: Space Physics*, *126*(11), e29851. https://doi.org/10.1029/2021JA029851

Auster, H. U., Glassmeier, K. H., Magnes, W., Aydogar, O., Baumjohann, W., Constantinescu, D., et al. (2008). The THEMIS fluxgate magnetometer. *Space Science Reviews*, *141*(1–4), 235–264. https://doi.org/10.1007/s11214-008-9365-9

Bashir, M. F., Artemyev, A., Zhang, X.-J., & Angelopoulos, V. (2022). Energetic electron precipitation driven by the combined effect of ULF, EMIC, and whistler waves. *Journal of Geophysical Research: Space Physics*, *127*(1), e29871. https://doi.org/10.1029/2021JA029871

Bentley, S. N., Stout, J. R., Bloch, T. E., & Watt, C. E. J. (2020). Random forest model of ultralow-frequency magnetospheric wave power. *Earth and Space Science*, *7*(10), e01274. https://doi.org/10.1029/2020EA001274

Bentley, S. N., Watt, C. E. J., Owens, M. J., & Rae, I. J. (2018). ULF wave activity in the magnetosphere: Resolving solar wind interdependencies to identify driving mechanisms. *Journal of Geophysical Research: Space Physics*, *123*(4), 2745–2771. https://doi.org/10.1002/2017JA024740

Brautigam, D. H., Ginet, G. P., Albert, J. M., Wygant, J. R., Rowland, D. E., Ling, A., & Bass, J. (2005). CRRES electric field power spectra and radial diffusion coefficients. *Journal of Geophysical Research*, *110*(A2), A02214. https://doi.org/10.1029/2004JA010612

Carpenter, D. L., & Anderson, R. R. (1992). An ISEE/whistler model of equatorial electron density in the magnetosphere. *Journal of Geophysical Research*, *97*(A2), 1097–1108. https://doi.org/10.1029/91JA01548

Chi, P. J., & Russell, C. T. (1998). Phase skipping and Poynting flux of continuous pulsations. *Journal of Geophysical Research*, *103*(A12), 29479–29492. https://doi.org/10.1029/98JA02101

Dai, L., Takahashi, K., Lysak, R., Wang, C., Wygant, J. R., Kletzing, C., et al. (2015). Storm time occurrence and spatial distribution of Pc4 poloidal ULF waves in the inner magnetosphere: A Van Allen probes statistical study. *Journal of Geophysical Research: Space Physics*, *120*(6), 4748–4762. https://doi.org/10.1002/2015JA021134

Degeling, A. W., Rae, I. J., Watt, C. E. J., Shi, Q. Q., Rankin, R., & Zong, Q. G. (2018). Control of ULF wave accessibility to the inner magnetosphere by the convection of plasma density. *Journal of Geophysical Research: Space Physics*, *123*(2), 1086–1099. https://doi.org/10.1002/2017JA024874

Degeling, A. W., & Rankin, R. (2008). Resonant drift echoes in electron phase space density produced by dayside Pc5 waves following a geomagnetic storm. *Journal of Geophysical Research*, *113*(A10), A10220. https://doi.org/10.1029/2008JA013254

Degeling, A. W., Rankin, R., Kabin, K., Rae, I. J., & Fenrich, F. R. (2010). Modeling ULF waves in a compressed dipole magnetic field. *Journal of Geophysical Research*, *115*(A10), A10212. https://doi.org/10.1029/2010JA015410

Di Matteo, S., & Villante, U. (2018). The identification of waves at discrete frequencies at the geostationary orbit: The role of the data analysis techniques and the comparison with solar wind observations. *Journal of Geophysical Research: Space Physics*, *123*(3), 1953–1968. https://doi.org/10.1002/2017JA024922

Di Matteo, S., Villante, U., Viall, N., Kepko, L., & Wallace, S. (2022). On differentiating multiple types of ULF magnetospheric waves in response to solar wind periodic density structures. *Journal of Geophysical Research: Space Physics*, *127*(3), e30144. https://doi.org/10.1029/2021JA030144

Drozdov, A. Y., Allison, H. J., Shprits, Y. Y., Elkington, S. R., & Aseev, N. A. (2021). A comparison of radial diffusion coefficients in 1-D and 3-D long-term radiation belt simulations. *Journal of Geophysical Research: Space Physics*, *126*(8), e28707. https://doi.org/10.1029/2020JA028707

Elkington, S. R., Hudson, M. K., & Chan, A. A. (1999). Acceleration of relativistic electrons via drift-resonant interaction with toroidal-mode Pc-5 ULF oscillations. *Geophysical Research Letters*, *26*(21), 3273–3276. https://doi.org/10.1029/1999GL003659

Elkington, S. R., Hudson, M. K., & Chan, A. A. (2003). Resonant acceleration and diffusion of outer zone electrons in an asymmetric geomagnetic field. *Journal of Geophysical Research*, *108*(A3), 1116. https://doi.org/10.1029/2001JA009202

Elkington, S. R., & Sarris, T. E. (2016). The role of pc-5 ULF waves in the radiation belts: Current understanding and open questions. In *Waves, particles, and storms in geospace: A complex interplay*. Oxford University Press. https://doi.org/10.1093/acprof:oso/9780198705246.003.0005

Elsden, T. (2023). Data for: 'properties of magnetohydrodynamic normal modes in the Earth's magnetosphere', by Hartinger et al., submitted to JGR space physics [Dataset]. figshare. https://doi.org/10.6084/m9.figshare.24433849.v1

Elsden, T., Wright, A., & Degeling, A. (2022). A review of the theory of 3-D Alfvén (field line) resonances. *Frontiers in Astronomy and Space Sciences*, *9*, 917817. https://doi.org/10.3389/fspas.2022.917817

Elsden, T., & Wright, A. N. (2019). The effect of fast normal mode structure and magnetopause forcing on FLRs in a 3-D waveguide. *Journal of Geophysical Research: Space Physics*, *124*(1), 178–196. https://doi.org/10.1029/2018JA026222

Elsden, T., & Wright, A. N. (2022). Polarization properties of 3-D field line resonances. *Journal of Geophysical Research: Space Physics*, *127*(2), e30080. https://doi.org/10.1029/2021JA030080

Fei, Y., Chan, A. A., Elkington, S. R., & Wiltberger, M. J. (2006). Radial diffusion and MHD particle simulations of relativistic electron transport by ULF waves in the September 1998 storm. *Journal of Geophysical Research*, *111*(A12), A12209. https://doi.org/10.1029/2005JA011211

Hartinger, M. D. (2023). THEMIS ULF power dataset [Dataset]. Zenodo. https://doi.org/10.5281/zenodo.7971722

Hartinger, M. D., Angelopoulos, V., Moldwin, M. B., Nishimura, Y., Turner, D. L., Glassmeier, K.-H., et al. (2012). Observations of a Pc5 global (cavity/waveguide) mode outside the plasmasphere by THEMIS. *Journal of Geophysical Research*, *117*(A6), A06202. https://doi.org/10.1029/2011JA017266

Hartinger, M. D., Angelopoulos, V., Moldwin, M. B., Takahashi, K., & Clausen, L. B. N. (2013). Statistical study of global modes outside the plasmasphere. *Journal of Geophysical Research: Space Physics*, *118*(2), 804–822. https://doi.org/10.1002/jgra.50140

Hartinger, M. D., Moldwin, M. B., Takahashi, K., Bonnell, J. W., & Angelopoulos, V. (2013). Survey of the ULF wave poynting vector near the Earth's magnetic equatorial plane. *Journal of Geophysical Research: Space Physics*, *118*(10), 6212–6227. https://doi.org/10.1002/jgra.50591

Hartinger, M. D., Shi, X., Rodger, C. J., Fujii, I., Rigler, E. J., Kappler, K., et al. (2023). Determining ULF wave contributions to geomagnetically induced currents: The important role of sampling rate. *Space Weather*, *21*(5), e2022SW003340. https://doi.org/10.1029/2022SW003340

Heyns, M. J., Lotz, S. I., & Gaunt, C. T. (2021). Geomagnetic pulsations driving geomagnetically induced currents. *Space Weather*, *19*(2), e2020SW002557. https://doi.org/10.1029/2020SW002557

Hughes, W. J., Southwood, D. J., Mauk, B., McPherron, R. L., & Barfield, J. N. (1978). Alfven waves generated by an inverted plasma energy distribution. *Nature*, *275*(5675), 43–45. https://doi.org/10.1038/275043a0

Jacobs, J. A., Kato, Y., Matsushita, S., & Troitskaya, V. A. (1964). Classification of geomagnetic micropulsations. *Journal of Geophysical Research*, *69*(1), 180–181. https://doi.org/10.1029/JZ069i001p00180

Kitamura, N., Shoji, M., Nakamura, S., Kitahara, M., Amano, T., Omura, Y., et al. (2021). Energy transfer between hot protons and electromagnetic ion cyclotron waves in compressional Pc5 ultra low frequency waves. *Journal of Geophysical Research: Space Physics*, *126*(5), e28912. https://doi.org/10.1029/2020JA028912

Kivelson, M. G., & Southwood, D. J. (1985). Resonant ULF waves: A new interpretation. *Geophysical Research Letters*, *12*(1), 49–52. https://doi.org/10.1029/GL012i001p00049

Kivelson, M. G., & Southwood, D. J. (1986). Coupling of global magnetospheric MHD eigenmodes to field line resonances. *Journal of Geophysical Research*, *91*(A4), 4345–4351. https://doi.org/10.1029/JA091iA04p04345

Laakso, H., & Pedersen, A. (1998). Ambient electron density derived from differential potential measurements. *Geophysical Monograph Series*, *102*, 49–54. https://doi.org/10.1029/GM102p0049

Lee, D.-H., & Kim, K. (1999). Compressional MHD waves in the magnetosphere: A new approach. *Journal of Geophysical Research*, *104*(A6), 12379–12386. https://doi.org/10.1029/1999JA900053

Lee, D.-H., & Lysak, R. L. (1989). Magnetospheric ULF wave coupling in the dipole model: The impulsive excitation. *Journal of Geophysical Research*, *94*(A12), 17097–17103. https://doi.org/10.1029/JA094iA12p17097

Lee, D.-H., & Lysak, R. L. (1990). Effects of azimuthal asymmetry on ULF waves in the dipole magnetosphere. *Geophysical Research Letters*, *17*(1), 53–56. https://doi.org/10.1029/GL017i001p00053

Lee, D.-H., & Takahashi, K. (2006). MHD eigenmodes in the inner magnetosphere. In *Magnetospheric ULF waves: Synthesis and new directions* (Vol. 169, p. 73). https://doi.org/10.1029/169GM07

Lejosne, S., & Kollmann, P. (2020). Radiation belt radial diffusion at Earth and beyond. *Space Science Reviews*, *216*(1), 19. https://doi.org/10.1007/s11214-020-0642-6

Lessard, M. R., Hudson, M. K., & Lühr, H. (1999). A statistical study of Pc3-Pc5 magnetic pulsations observed by the AMPTE/ion release module satellite. *Journal of Geophysical Research*, *104*(A3), 4523–4538. https://doi.org/10.1029/1998JA900116

Li, L., Omura, Y., Zhou, X.-Z., Zong, Q.-G., Rankin, R., Yue, C., & Fu, S.-Y. (2022). Nonlinear wave growth analysis of chorus emissions modulated by ULF waves. *Geophysical Research Letters*, *49*(10), e97978. https://doi.org/10.1029/2022GL097978

Li, W., Thorne, R. M., Bortnik, J., Nishimura, Y., & Angelopoulos, V. (2011). Modulation of whistler mode chorus waves: 1. Role of compressional Pc4-5 pulsations. *Journal of Geophysical Research*, *116*(A6), A06205. https://doi.org/10.1029/2010JA016312

Mann, I. R., Chisham, G., & Bale, S. D. (1998). Multisatellite and ground-based observations of a tailward propagating Pc5 magnetospheric waveguide mode. *Journal of Geophysical Research*, *103*(A3), 4657–4670. https://doi.org/10.1029/97JA03175

Matzka, J., Stolle, C., Yamazaki, Y., Bronkalla, O., & Morschhauser, A. (2021). The geomagnetic Kp index and derived indices of geomagnetic activity. *Space Weather*, *19*(5), e2020SW002641. https://doi.org/10.1029/2020SW002641

McFadden, J. P., Carlson, C. W., Larson, D., Bonnell, J., Mozer, F., Angelopoulos, V., et al. (2008). THEMIS ESA first science results and performance issues. *Space Science Reviews*, *141*(1–4), 477–508. https://doi.org/10.1007/s11214-008-9433-1

McFadden, J. P., Carlson, C. W., Larson, D., Ludlam, M., Abiad, R., Elliott, B., et al. (2008). The THEMIS ESA plasma instrument and in-flight calibration. *Space Science Reviews*, *141*(1–4), 277–302. https://doi.org/10.1007/s11214-008-9440-2

Moore, T. E., Gallagher, D. L., Horwitz, J. L., & Comfort, R. H. (1987). MHD wave breaking in the outer plasmasphere. *Geophysical Research Letters*, *14*(10), 1007–1010. https://doi.org/10.1029/GL014i010p01007

Murphy, K. R., Mann, I. R., & Sibeck, D. G. (2015). On the dependence of storm time ULF wave power on magnetopause location: Impacts for ULF wave radial diffusion. *Geophysical Research Letters*, *42*(22), 9676–9684. https://doi.org/10.1002/2015GL066592

O'Brien, T. P., & Moldwin, M. B. (2003). Empirical plasmapause models from magnetic indices. *Geophysical Research Letters*, *30*(4), 1152. https://doi.org/10.1029/2002GL016007

Ozeke, L. G., Mann, I. R., Murphy, K. R., Jonathan Rae, I., & Milling, D. K. (2014). Analytic expressions for ULF wave radiation belt radial diffusion coefficients. *Journal of Geophysical Research: Space Physics*, *119*(3), 1587–1605. https://doi.org/10.1002/2013JA019204

Plaschke, F., & Glassmeier, K. H. (2011). Properties of standing Kruskal-Schwarzschild-modes at the magnetopause. *Annales Geophysicae*, *29*(10), 1793–1807. https://doi.org/10.5194/angeo-29-1793-2011

Rae, I. J., Mann, I. R., Watt, C. E. J., Kistler, L. M., & Baumjohann, W. (2007). Equator-S observations of drift mirror mode waves in the dawnside magnetosphere. *Journal of Geophysical Research*, *112*(A11), A11203. https://doi.org/10.1029/2006JA012064

Samson, J. C., Harrold, B. G., Ruohoniemi, J. M., Greenwald, R. A., & Walker, A. D. M. (1992). Field line resonances associated with MHD waveguides in the magnetosphere. *Geophysical Research Letters*, *19*(5), 441–444. https://doi.org/10.1029/92GL00116

Sandhu, J. K., Rae, I. J., Staples, F. A., Hartley, D. P., Walach, M. T., Elsden, T., & Murphy, K. R. (2021). The roles of the magnetopause and plasmapause in storm-time ULF wave power enhancements. *Journal of Geophysical Research: Space Physics*, *126*(7), e29337. https://doi.org/10.1029/2021JA029337

Sandhu, J. K., Rae, I. J., Wygant, J. R., Breneman, A. W., Tian, S., Watt, C. E. J., et al. (2021). ULF wave driven radial diffusion during geomagnetic storms: A statistical analysis of Van Allen probes observations. *Journal of Geophysical Research: Space Physics*, *126*(4), e29024. https://doi.org/10.1029/2020JA029024

Sarris, T. E., Li, X., Zhao, H., Papadakis, K., Liu, W., Tu, W., et al. (2022). Distribution of ULF wave power in magnetic latitude and local time using THEMIS and Arase measurements. *Journal of Geophysical Research: Space Physics*, *127*(10), e2022JA030469. https://doi.org/10.1029/2022JA030469

Shi, X., Baker, J. B. H., Ruohoniemi, J. M., Hartinger, M. D., Frissell, N. A., & Liu, J. (2017). Simultaneous space and ground-based observations of a plasmaspheric virtual resonance. *Journal of Geophysical Research: Space Physics*, *122*(4), 4190–4209. https://doi.org/10.1002/2016JA023583

Shi, X., Zhang, X.-J., Artemyev, A., Angelopoulos, V., Hartinger, M. D., Tsai, E., & Wilkins, C. (2022). On the role of ULF waves in the spatial and temporal periodicity of energetic electron precipitation. *Journal of Geophysical Research: Space Physics*, *127*(12), e2022JA030932. https://doi.org/10.1029/2022JA030932

Shue, J. H., Chao, J. K., Fu, H. C., Russell, C. T., Song, P., Khurana, K. K., & Singer, H. J. (1997). A new functional form to study the solar wind control of the magnetopause size and shape. *Journal of Geophysical Research*, *102*(A5), 9497–9512. https://doi.org/10.1029/97JA00196

Southwood, D. J. (1974). Some features of field line resonances in the magnetosphere. *Planetary and Space Science*, *22*(3), 483–491. https://doi.org/10.1016/0032-0633(74)90078-6

Southwood, D. J., & Hughes, W. J. (1983). Theory of hydromagnetic waves in the magnetosphere. *Space Science Reviews*, *35*(4), 301–366. https://doi.org/10.1007/BF00169231

Sugiura, M., & Wilson, C. R. (1964). Oscillation of the geomagnetic field lines and associated magnetic perturbations at conjugate points. *Journal of Geophysical Research*, *69*(7), 1211–1216. https://doi.org/10.1029/JZ069i007p01211

Takahashi, K., & Anderson, B. J. (1992). Distribution of ULF energy (f<=80 mHz) in the inner magnetosphere: A statistical analysis of AMPTE CCE magnetic field data. *Journal of Geophysical Research*, *97*(A7), 10751–10773. https://doi.org/10.1029/92JA00328

Takahashi, K., Bonnell, J., Glassmeier, K.-H., Angelopoulos, V., Singer, H. J., Chi, P. J., et al. (2010). Multipoint observation of fast mode waves trapped in the dayside plasmasphere. *Journal of Geophysical Research*, *115*(A12), A12247. https://doi.org/10.1029/2010JA015956

Takahashi, K., Hartinger, M. D., Angelopoulos, V., & Glassmeier, K.-H. (2015). A statistical study of fundamental toroidal mode standing Alfvén waves using THEMIS ion bulk velocity data. *Journal of Geophysical Research: Space Physics*, *120*(8), 6474–6495. https://doi.org/10.1002/2015JA021207

Takahashi, K., McPherron, R. L., & Terasawa, T. (1984). Dependence of the spectrum of Pc 3-4 pulsations on the interplanetary magnetic field. *Journal of Geophysical Research*, *89*(A5), 2770–2780. https://doi.org/10.1029/JA089iA05p02770

Takahashi, K., & Ukhorskiy, A. Y. (2007). Solar wind control of Pc5 pulsation power at geosynchronous orbit. *Journal of Geophysical Research*, *112*(A11), A11205. https://doi.org/10.1029/2007JA012483

Tamao, T. (1965). Transmission and coupling resonance of hydromagnetic disturbances in the non-uniform Earth's magnetosphere. *Science reports of the Tohoku University. Series 5, Geophysics*, *17*, 43–70.

Watt, C. E. J., Degeling, A. W., Rankin, R., Murphy, K. R., Rae, I. J., & Singer, H. J. (2011). Ultralow-frequency modulation of whistler-mode wave growth. *Journal of Geophysical Research*, *116*(A10), A10209. https://doi.org/10.1029/2011JA016730

Wharton, S. J., Wright, D. M., Yeoman, T. K., James, M. K., & Sandhu, J. K. (2019). The variation of resonating magnetospheric field lines with changing geomagnetic and solar wind conditions. *Journal of Geophysical Research: Space Physics*, *124*(7), 5353–5375. https://doi.org/10.1029/2019JA026848

Wright, A. N., & Elsden, T. (2020). Simulations of MHD wave propagation and coupling in a 3-D magnetosphere. *Journal of Geophysical Research: Space Physics*, *125*(2), e27589. https://doi.org/10.1029/2019JA027589

Wright, A. N., & Mann, I. R. (2006). Global MHD eigenmodes of the outer magnetosphere. In *Magnetospheric ulf waves: Synthesis and new directions* (Vol. 169, p. 51). https://doi.org/10.1029/169GM06

Xia, Z., Chen, L., Dai, L., Claudepierre, S. G., Chan, A. A., Soto-Chavez, A. R., & Reeves, G. D. (2016). Modulation of chorus intensity by ULF waves deep in the inner magnetosphere. *Geophysical Research Letters*, *43*(18), 9444–9452. https://doi.org/10.1002/2016GL070280

Xia, Z., Chen, L., & Li, W. (2020). Statistical study of chorus modulations by background magnetic field and plasma density. *Geophysical Research Letters*, *47*(22), e89344. https://doi.org/10.1029/2020GL089344

Zhang, D., Liu, W., Zhang, Z., Li, X., Sarris, T. E., Goldstein, J., & Dmitry, R. (2023). Cavity mode wave frequency variation associated with inward motion of the magnetopause during interplanetary shock compression. *Journal of Geophysical Research: Space Physics*, *128*(3), e2023JA031299. https://doi.org/10.1029/2023JA031299

Zhang, X. J., Angelopoulos, V., Artemyev, A. V., Hartinger, M. D., & Bortnik, J. (2020). Modulation of whistler waves by ultra-low-frequency perturbations: The importance of magnetopause location. *Journal of Geophysical Research: Space Physics*, *125*(10), e28334. https://doi.org/10.1029/2020JA028334

Zhang, X.-J., Chen, L., Artemyev, A. V., Angelopoulos, V., & Liu, X. (2019). Periodic excitation of chorus and ECH waves modulated by ultra-low frequency compressions. *Journal of Geophysical Research: Space Physics*, *124*(11), 8535–8550. https://doi.org/10.1029/2019JA027201

Zhu, X., & Kivelson, M. G. (1991). Compressional ULF waves in the outer magnetosphere 1. Statistical study. *Journal of Geophysical Research*, *96*(A11), 19451–19467. https://doi.org/10.1029/91JA01860

Zong, Q., Rankin, R., & Zhou, X. (2017). The interaction of ultra-low-frequency Pc3-5 waves with charged particles in Earth's magnetosphere. *Reviews of Modern Plasma Physics*, *1*, 10. https://doi.org/10.1007/s41614-017-0011-4